

2015-01-01

# Fluid Flow Characterization of High Turbulent Intensity Compressible Flow Using Particle Image Velocimetry

Marco Efrain Quiroz

University of Texas at El Paso, examC@yahoo.com

Follow this and additional works at: [https://digitalcommons.utep.edu/open\\_etd](https://digitalcommons.utep.edu/open_etd)



Part of the [Mechanical Engineering Commons](#)

---

## Recommended Citation

Quiroz, Marco Efrain, "Fluid Flow Characterization of High Turbulent Intensity Compressible Flow Using Particle Image Velocimetry" (2015). *Open Access Theses & Dissertations*. 1128.  
[https://digitalcommons.utep.edu/open\\_etd/1128](https://digitalcommons.utep.edu/open_etd/1128)

This is brought to you for free and open access by DigitalCommons@UTEP. It has been accepted for inclusion in Open Access Theses & Dissertations by an authorized administrator of DigitalCommons@UTEP. For more information, please contact [lweber@utep.edu](mailto:lweber@utep.edu).

FLUID FLOW CHARACTERIZATION OF HIGH TURBULENT INTENSITY  
COMPRESSIBLE FLOW USING PARTICLE IMAGE VELOCIMETRY

MARCO EFRAIN QUIROZ-REGALADO

Department of Mechanical Engineering

APPROVED:

---

Ahsan R. Choudhuri, Ph.D., Chair

---

Evgeny Shafirovich, Ph.D.

---

Tzu-Liang (Bill) Tseng, Ph.D.

---

Charles Ambler, Ph.D.  
Dean of the Graduate School

Copyright ©

by

Marco Efrain Quiroz

2015

## **Dedication**

To my mother and sister, the two people who've done more for me than anyone else ever will.

FLUID FLOW CHARACTERIZATION OF HIGH TURBULENT INTENSITY  
COMPRESSIBLE FLOW USING PARTICLE IMAGE VELOCIMETRY

by

MARCO EFRAIN QUIROZ, BSME

THESIS

Presented to the Faculty of the Graduate School of

The University of Texas at El Paso

in Partial Fulfillment

of the Requirements

for the Degree of

MASTER OF SCIENCE

Department of Mechanical Engineering

THE UNIVERSITY OF TEXAS AT EL PASO

August 2015

## **Acknowledgements**

I would like to express my gratitude and appreciation to Dr. Choudhuri, whose leadership, support, and vision made this project possible. I would also like to thank Abraham Trujillo and Scott Hill for all their help and guidance which proved to be crucial for the completion of this thesis. I would also like to acknowledge all the cSETR faculty and staff for their support and contributions, as well as my invaluable teammates; Arif Hossain, Arturo Acosta, and Martin De La Torre. These individuals are among the best that the cSETR has to offer, and it was a privilege to be working with them. Finally, I would like to acknowledge the financial support provided by NASA under award No(s) NNX09AV09A and W911NF-13-1-0156 via the Army Research Office (ARO).

## Abstract

A high turbulent intensity combustion chamber has been designed in order to operate with compressible ( $0.3 < M < 0.5$ ) and preheated ( $T=500\text{K}$ ) air-methane combustion. These conditions will allow the investigation of different flame regimes; most notably the proposed ‘Thickened Flame’ regime. Initial design and flow validation has been completed in order to begin further experimentation. A 10 kHz Time Resolved Particle Image Velocimetry (TR-PIV) system and a 3 kHz Planer Laser Induced Fluorescence (PLIF) system have been integrated with the system in order to diagnose the flow field and the flame respectively. The exhaust and chamber cooling subsystems were designed to comply with safety regulations, and the control systems were set up in a way that allows automated (LabVIEW) and user controlled sequencing. This work’s main purpose is to characterize and map the flow properties at maximum flow conditions ( $M > 0.3$ ) in order to map the following; flow structures, kinetic energy at different length scales, velocity fluctuations and turbulent intensity. PIV measurements are carried out for three different volumetric flow rates ( $\dot{V} = 25 \text{ scfm}$ ,  $55 \text{ scfm}$ , and  $115 \text{ scfm}$ ) and three different grid geometries for each (BR= 67%, 61%, and 54%). Upon finding that the main flow structure consisted of jets caused by the grid at higher flowrates, experiments were done with a grid BR = 67% which was thinner (50% of original thickness) than the previously used grids. The thinner grid produced structures which showed flow breakup not seen previously due to the jets, however the grid BR = 61% showed best overall flow structure. The experimental results allowed the velocity fluctuation and length scale terms to be quantified and can be used with future flame studies to determine flame regime location according to the Borghi-Peters diagram.

# Table of Contents

Acknowledgements.....	v
Abstract.....	vi
Table of Contents.....	vii
List of Tables .....	ix
List of Figures .....	x
Chapter 1: Introduction .....	1
1.1    Objective.....	2
Chapter 2: Theory and Literature Review.....	3
2.1    Flow over a Backward-Facing Step.....	3
2.2    Turbulent Flow.....	4
2.2.1    General Description of Turbulence.....	5
2.3    Optical Diagnostics.....	8
2.3.1    Particle Image Velocimetry (PIV) .....	9
2.3.2    Planar Laser Induced Fluorescence (PLIF).....	10
2.4    Flame Regimes.....	13
Chapter 3: Experimental Setup .....	16
3.1    System description .....	16
3.2    Air Preheating .....	21
3.3    Exhaust Design .....	24
3.4    Combustion Chamber Cooling.....	26
3.5    Control System.....	29
3.7    Test Setup Summary .....	32
Chapter 4: Methodology .....	33
Chapter 5: Result and Discussion .....	38
5.1    Particle Image Velocimetry (PIV) Testing .....	39
5.1.1    Proper Orthogonal Decomposition Results.....	40
5.1.2    Measurement of Kinetic Energy .....	45
5.1.3    Measurement of Turbulent Intensity.....	48
5.1.4    Comparison of Grid Thickness .....	51



Chapter 6: Conclusion and Future Work .....	53
6.1    Summary .....	53
6.2    Future Work .....	54
References.....	55
Appendix I .....	58
Appendix II .....	62
Appendix III.....	65
Appendix IV.....	67
Glossary .....	70
Vita.....	71

## **List of Tables**

Table 2.1: Reynolds number characterization for different flows .....	4
Table 2.2: Absorption wavelengths for different combustion species .....	12
Table 3.1 System Requirements.....	16
Table 3.2: Components in combustor and their factor of safety .....	18
Table 3.3: Comparison between theoretical and CFD results .....	25
Table 3.4: DAC controlled instrumentation.....	29
Table 3.5: A summarization of the subsystems that make up the high turbulent intensity system.....	32
Table 4.1: Test matrix for fluid flow studies .....	33
Table 4.2: Grid description .....	37
Table 5.1: Summarization of flow condition results .....	39

## List of Figures

Figure 2.1: Fluid behavior over a backward-facing step [2] .....	3
Figure 2.2: Plot showing variation in velocity measurement for a turbulent flow [9] .....	5
Figure 2.3: Visual representation of the energy dissipation in a turbulent flow .....	7
Figure 2.4: Visual representation of grid induced turbulence in a duct .....	8
Figure 2.5: General PIV setup [16] .....	10
Figure 2.6: Visual representation of molecular activity after energy absorption [17] .....	11
Figure 2.7: OH, CH, and CH <sub>2</sub> O imaging for a simple jet [19] .....	12
Figure 2.8: Flame regime diagram by Borghi and modified by Peter .....	13
Figure 2.9: Different flame regimes and the graphical illustrations of flame front characteristics .....	14
Figure 3.1: Exploded model of the combustor subsystem and its components .....	17
Figure 3.2: Cross-sectional view of the combustor showing 2D plane used in simulations [5] .....	18
Figure 3.3: Flow schematic of the combustion system and detailed pilot flame flow schematic .....	19
Figure 3.4: Combustion chamber showing location of pilot flames .....	20
Figure 3.5: LS1 coil wiring diagram .....	20
Figure 3.6: Heater (a) model with stand and (b) manufacturer specific drawing .....	21
Figure 3.7: Inconel heating elements inside the heater .....	22
Figure 3.8: Static temperature contours of preheated air .....	23
Figure 3.9: Plot of steady state, transient, and average temperature profiles at heater exit .....	23
Figure 3.10: Initial conceptual model of exhaust section with spray nozzle diagram .....	24
Figure 3.11: Temperature contours in exhaust simulation .....	26
Figure 3.12: CAD model of heat exchanger and dynalene tank (left) and physical setup (right) .....	27
Figure 3.13: Additional schematic of heat exchanger used for cooling .....	28
Figure 3.14: Temperature vs time plots for critical thickness and largest quartz window .....	28
Figure 3.15: Main control box .....	30

Figure 3.16: Electrical schematic of main control box .....	30
Figure 3.17: LabVIEW control panel interface.....	31
Figure 3.18: DAQ assist block diagram.....	31
Figure 4.1: Flow schematic of the present study.....	33
Figure 4.2: Raw PIV image showing calibration .....	34
Figure 4.3: Raw image detailing the different components in the PIV capture .....	35
Figure 4.4: Solenoid valve (a), proportional control valve (b) and flowmeter (c).....	36
Figure 4.5: PIV system being fired into the combustor for flow analysis .....	36
Figure 4.6: Main airline left and mixing chamber with seeding point indicated (right) .....	37
Figure 5.1: Average u velocity profile after grid comparison between CFD and PIV results [28] .....	38
Figure 5.2: comparison of PIV images and CFD results for RE = 850 .....	38
Figure 5.3: Area of interest for PIV analysis with lines indicating location of data extraction .....	40
Figure 5.4: Sample POD snapshot for BR 67% and Re = 22321 .....	41
Figure 5.5: POD projection with 67% BR and Re = 22321.....	41
Figure 5.6: POD projection with 67% BR and Re = 10765.....	42
Figure 5.7: POD projection with 61% BR and Re = 24413.....	42
Figure 5.8: POD projection with 61% BR and Re = 11676.....	43
Figure 5.9: POD projection with 54% BR and Re = 26506.....	43
Figure 5.10: POD projection with 54% BR and Re = 12676.....	44
Figure 5.11: Kinetic energy distribution in the flow shown for 67% BR at Re = 22321.....	45
Figure 5.12: Normalized kinetic energy before the step for BR = 54%, 61% and 67% at Re = 12676, 11676 and 10675 respectively.....	46
Figure 5.13: Normalized kinetic energy before step for 67% and 61% BR at 22321 and 24413 respectively .....	46
Figure 5.14: Normalized kinetic energy after the step for BR = 54%, 61% and 67% at Re = 12676, 11676 and 10675 respectively .....	47

Figure 5.15: Normalized kinetic energy after the step for BR = 54%, 61% and 67% at Re = 26506, 24413 and 22321 respectively .....	47
Figure 5.16: Turbulent intensity before step with BR = 54%, 61% and 67% and Re = 12676, 11676 and 10675 respectively .....	48
Figure 5.17: Turbulent intensity before step for BR = 67% and 61% with Re = 24413 and 22321 respectively .....	49
Figure 5.18: Turbulent intensity after the step with BR = 54%, 61% and 67% and Re = 12676, 11676 and 10675 respectively .....	49
Figure 5.19: Turbulent intensity after the step with BR = 54%, 61% and 67% and Re = 26506, 24413 and 22321 respectively .....	50
Figure 5.20: POD projection of thin grid BR = 67% and Re = 22321 .....	51
Figure 5.21: Normalized kinetic energy for regular and thin grid at BR = 67% and Re = 22321 .....	52
Figure 5.22: Turbulent intensity comparison between regular and thin 67% BR at Re = 22321 .....	52

## **Chapter 1: Introduction**

The fundamental understanding of turbulent premixed combustion is one of the major research topics of interest in the industry and it has become one of the prior research interests of the Air Force Office of Scientific Research (AFSOR). Many experiments aim to successfully study flames at highly turbulent conditions in order to gain a better understanding in turbine design and emissions control. There have been many studies which aim to provide useful data in this topic, but there are still many uncertainties associated with turbulent combustion. Designers still rely on the design-test-modify method which is not only time consuming but also expensive. It is because of this that the industrial community is searching for a reliable and effective numerical model in order to design next generation combustors, and these models need a detailed experimental analysis of the fundamentals of turbulent flame structure and a wide range of experimental data in order to be valid design methods.

The development of high repetition rate laser diagnostic techniques such as Particle Image Velocimetry (PIV) and Laser Induced Fluorescence (LIF) enable the study of turbulent flow and turbulent combustion. These non-intrusive techniques provide a way to study the actual high speed flow with minimal effect to the flow field. A safe and reliable high intensity combustion system has been developed in order to:

- Study the characteristics of premixed flame structure at compressible and high turbulent intensity conditions.
- Experimentally establish the limits of flame regime boundaries under these conditions.
- Generate experimental data through the use of simultaneous PIV and PLIF.
- Generate experimental data to quantify turbulent flow characteristics.

The main goal of this study is to complete the characterization and mapping of the fluid flow at several flow rates, including maximum operating conditions ( $\text{Mach} > 0.3$ ). System validation has been conducted and the next objective is to increase the operating conditions in

order to have a full understanding of the flow interactions inside the combustion chamber. Different flow rates and grid geometries are used in order to have a wide range of data sets.

## **1.1 Objective**

The Center for Space Exploration Technology Research (cSETR) at the University of Texas at El Paso specializes in propulsion and combustion research. Of the many instruments available in the center, is a 10 kHz Particle Image Velocimetry (PIV) and a 3 kHz Planer Laser Induced Fluorescence (PLIF) system. The facility also has 3 kHz high speed imaging system and a compressor system which can supply 190 scfm of air at a supply pressure of 140 psi. This specific experiment is supported by the Army Research Office (ARO) and a collaboration with Princeton University. The main objectives of this project are proposed as following:

- To study the global characteristics of a backward facing step stabilized flame in compressible and high intensity turbulent flow using high speed flow visualization technology.
- To study flow and flame characteristics using Time Resolved Particle Image Velocimetry (TR-PIV) and OH/CH Planer Laser Induced Fluorescence (PLIF) imaging.
- To generate components of turbulent intensity and turbulent kinetic energy.
- To define the effects of bulk velocity parameters, turbulence parameters and recirculation zone characteristics on flame location, shape, fluctuation, reaction zone and local displacement speed.

The preliminary tasks of designing and validating the system have been completed, and the main objectives can now be completed. At this stage, the main objective is to do a complete study of the flow characteristics using the PIV system. Various flow rates and grid geometries are studied and presented in order to determine which turbulator (grid) generates the best flow structures.

## Chapter 2: Theory and Literature Review

### 2.1 Flow over a Backward-Facing Step

The backward facing step is a well-studied phenomenon in fluid mechanics, and its flow characteristics is what will be used in order to stabilize the highly turbulent flame. The fluid behavior due to a backward facing step geometry has been characterized over the years and this fluid behavior can be seen in Figure 2.1. Early studies were conducted using laminar flow in order to develop a method for resolving the issues of a backward facing step through the use of computational methods [1]. Later, more thorough studies were performed by Biswas et al [3] and Armaly et al [4] to further the understanding of the backward facing step different, more turbulent conditions. Extensive studies were also conducted by Yuan and So [2], which included more characterization parameters in a simple flow over a backward facing step. Several fluid characteristics which occur in this geometry can now be modeled more accurately and for higher turbulent conditions.

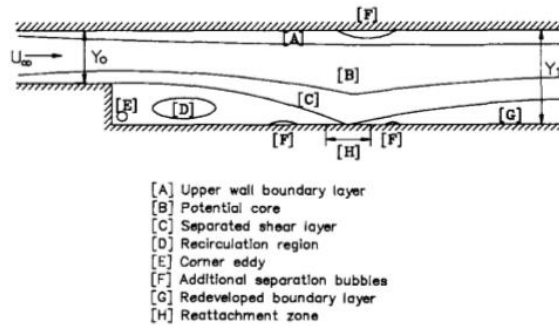


Figure 2.1: Fluid behavior over a backward-facing step [2]

Flow simulations for the present study were completed and validated in previous works [5]. A Large Eddy Simulation (LES) model was used in order to identify the flow structures (recirculation, reattachment length, and length scales) and characteristics for this geometry. Further discussion regarding initial flow validation is found in Chapter 3.



## 2.2 Turbulent Flow

Turbulence in fluid mechanics refers to flow which is unpredictable, unsteady and chaotic. Turbulence is also used in combustion applications since it offers better mixing of reactants. It is important to understand Turbulence in order to correctly characterize and map the flow field in this project.

The most basic way of determining the turbulence of a certain flow is through the use of the Reynolds number. The term derives from fluid mechanics pioneer Osborne Reynolds [7]. The Reynolds number represents a dimensionless parameter which considers the ratio of inertial to viscous forces and serves to determine the dominant force that influences the fluid's behavior. Equation 2.1 shows the mathematical representation of this term.

$$Re = \frac{UL}{\nu} \quad (2.1)$$

In this equation  $U$ ,  $L$ , and  $\nu$  represent the characteristic velocity, characteristic length, and fluid kinematic viscosity respectively [6]. Different ranges in the Reynolds number determine whether the flow is considered laminar or turbulent. Simply speaking, the faster the velocity of a fluid, then the more dominant the inertial forces are compared to the 'slowing' caused by viscosity. Table 2.1 shows how laminar and turbulent flows are characterized for different conditions.

Table 2.1: Reynolds number characterization for different flows

	Reynolds number
Laminar	$Re \leq 2300$
Transitional	$2300 < Re < 4000$
Turbulent	$Re \geq 4000$

While a higher Reynolds number generally indicates higher turbulence, the transition region serves to accommodate cases where material roughness or obstructions in the flow may affect flow development.

### 2.2.1 GENERAL DESCRIPTION OF TURBULENCE

The characteristics and aspects of turbulent flow are described in thorough detail by the work of Pope [9]. As mentioned in the previous section, turbulent flow exhibits unpredictability and chaos. Figure 2.2 shows a plot of the velocity at different time intervals of a turbulent flow.

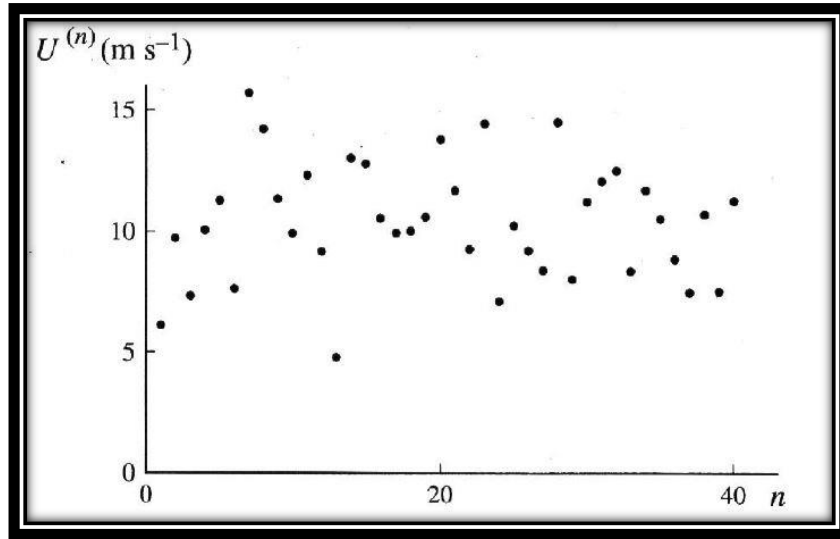


Figure 2.2: Plot showing variation in velocity measurement for a turbulent flow [9]

In order to characterize the characteristics of turbulence in the flow, the velocity must be resolved into two components; mean and fluctuation as shown in Equation 2.2.

$$u(t) = \bar{u} + u'(t) \quad (2.2)$$

$$u'(t) = u(t) - \bar{u} \quad (2.3)$$

The mean velocity  $\bar{u}$  can be calculated by taking an average velocity measurement for a certain time interval which is much larger than the turbulent time scale [10]. From the velocity fluctuation, it is then possible to calculate the root mean square (r.m.s.) value of this turbulence component.

$$u_{rms} = sdev(u'(t)) = \sqrt{var(u'(t))} = \sqrt{u'(t)^2} \quad (2.4)$$

## **Turbulent Intensity**

Turbulent intensity is a parameter used to quantify the turbulence of a flow field and is generally expressed as a percentage.

$$I = \frac{u_{rms}}{\bar{u}} \quad (2.5)$$

In an ideal flow (i.e. non turbulent), the  $u_{rms}$  value would be 0, therefore the turbulent intensity is also 0%. The turbulent intensity in high speed flows is generally over 10%. This variable is one of the crucial variables in mapping the flow field for the present work.

## **Turbulent Kinetic Energy**

Similar to kinetic energy (KE), the turbulent kinetic energy (TKE) is a measure of energy per unit mass due to the velocity in a flow. Though in order to calculate TKE, as opposed to KE, the fluctuation component of velocity is used as follows-

$$TKE = \frac{1}{2} ( \overline{u'^2} + \overline{v'^2} + \overline{w'^2} ) = \frac{3}{2} \overline{u'^2} \quad (2.6)$$

Again, the r.m.s. value of the velocity fluctuation is used to calculate this variable [9].

## **Turbulent Length Scale**

When dealing with turbulent flow, the characterization of energy modes and length scales is crucial to mapping flow fields. As flow becomes turbulent, viscous effects bring about the formation of energy dissipating eddies. These eddies provide a way to determine the length scales in a flow. The largest scale eddy is one which carries the largest amount of energy in a flow, and this energy is dissipated into smaller eddies until energy is simply dissipated as heat. Richardson and Kolmogorov introduced and refined the theory of what is known as the ‘energy cascade’ and ‘Kolmogorov hypothesis’ which explain this phenomenon [9]. The energy cascade can be summed up in the following:

Big whorls have little whorls,  
Which feed on their velocity;  
And little whorls have lesser whorls,  
And so on to viscosity (in the molecular sense) [11]

Kolmogorov then introduced a method to quantifying these parameters to be universal and applicable to all flows. The energy dissipation starts at the largest scale  $L$ , to the smallest scale  $\eta$  as shown in Figure 2.3. Once energy reaches the dissipation range, the smallest scales of length, time, and velocity can be calculated based on the viscosity of the fluid. These small scale parameters are defined as follows-

$$\eta = \left(\frac{\nu^3}{\varepsilon}\right)^{\frac{1}{4}} \quad (2.7)$$

$$t_\eta = \left(\frac{\nu}{\varepsilon}\right)^{1/2} \quad (2.8)$$

$$u_\eta = (\varepsilon \nu)^{1/4} \quad (2.9)$$

$$\varepsilon \equiv \frac{u_0^3}{L} \quad (2.10)$$

Here  $\varepsilon$  represents the energy dissipation which scales according to the characteristic velocity,  $u_0$  and length scale. It can be seen that the smallest scales are defined by the kinematic viscosity  $\nu$  of the fluid and the energy dissipation  $\varepsilon$ . Using Equation 2.8, we can find the time interval used to average the velocity in Equation 2.2 and 2.3 in order to correctly calculate the mean and fluctuation velocity components.

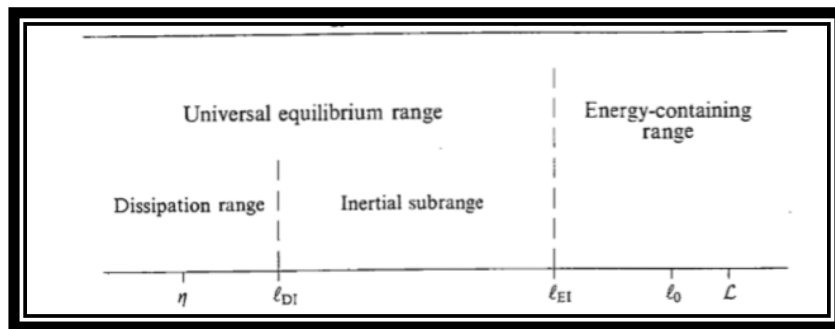


Figure 2.3: Visual representation of the energy dissipation in a turbulent flow

### Grid Induced Turbulence

The use of a wire mesh, usually referred to as a grid, can be used to induce turbulence in a cross-flow. This can cause the flow to become more turbulent, and thus is a common method to induce turbulence in a flow. The grid creates homogenous turbulence which increases with time

by  $t = x/U_0$ , and decays along the x-direction. The use of a grid shows that the r.m.s. value of the x-component of the velocity is 10% greater than the y-direction component [9]. The flow begins to exhibit transitional turbulence at the point where the grid is, and gradually develops into a fully developed turbulent flow. As the flow progresses axially the flow begins to decay, starting with the smallest scale eddies. A visual representation of grid induced turbulence can be seen in Figure 2.4. In the present study, three different perforated plates are used in order to increase the turbulence and effectively increase the velocity fluctuation and turbulent intensity.

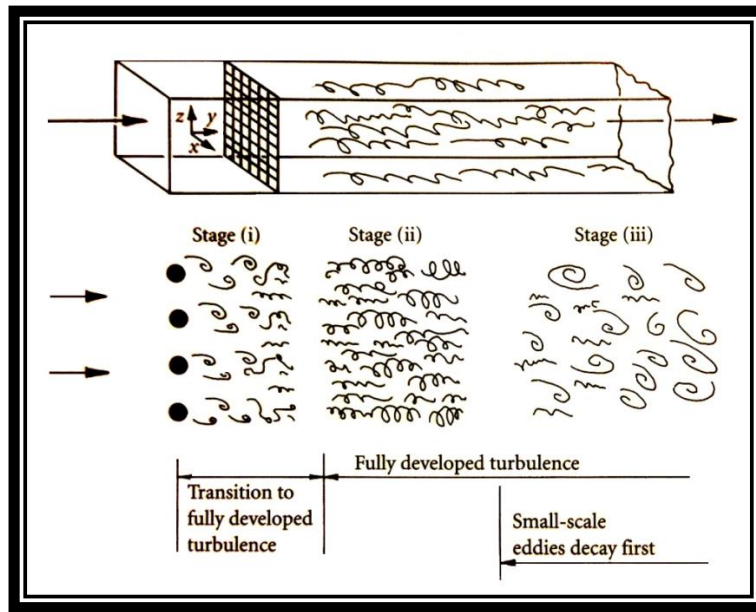


Figure 2.4: Visual representation of grid induced turbulence in a duct

## 2.3 Optical Diagnostics

Laser imaging techniques provide a non-intrusive way of measuring flow parameters, combustion, emissions and all their individual components. Optical diagnostics began as early as the 1800's, but were popularized in the early 20<sup>th</sup> century and are now widely used in turbulent combustion research [14]. There are a wide variety of imaging techniques and systems, and in the present study a PIV and LIF system are to be used. These systems are to be run separately, as well as simultaneously.

### 2.3.1 PARTICLE IMAGE VELOCIMETRY (PIV)

Particle Image Velocimetry (PIV) is a way to map flow characteristics such as velocity vector fields, vorticity, strain and divergence of the flow. In general, a PIV system consists of the following three important components; seeding particles or other flow tracer, a high powered laser, and a CCD camera. The works of Adrain [15] explain the working of a PIV system and is therefore a useful resource to help understand some basic concepts. PIV systems are usually complemented with software which generates all the desired parameters based on particle movement. It utilizes the captured images from the camera to determine the velocity components by measuring the calibrated displacement of a single particle over a specified time step. Images are recorded and paired in order to have a ‘first’ and ‘second’ image which the displacement can be calculated from.

$$u = \frac{\Delta x}{\Delta t} \quad (2.11)$$

$$v = \frac{\Delta y}{\Delta t} \quad (2.12)$$

PIV accuracy depends on successful synchronization of image capture and laser firing as well as proper calibration and image capture quality. The correct use of particles is also paramount to obtaining useful data. Particles should be sufficient enough to be traced by the camera from one image frame to the next, but also sparse enough to not over-saturate the image. A relation between particle and fluid properties can be used to have adequate sizing and volumetric concentration of particles. This can be seen by-

$$\frac{\rho_p \pi d_p^4 v_r}{18 \pi \delta_p^3} < 1 \quad (4.2)$$

Where  $d_p$ ,  $v_r$ ,  $\delta_p$ , and  $\rho_p$  are the particle diameter, fluid viscosity, average distance between particles, and particle density respectively.

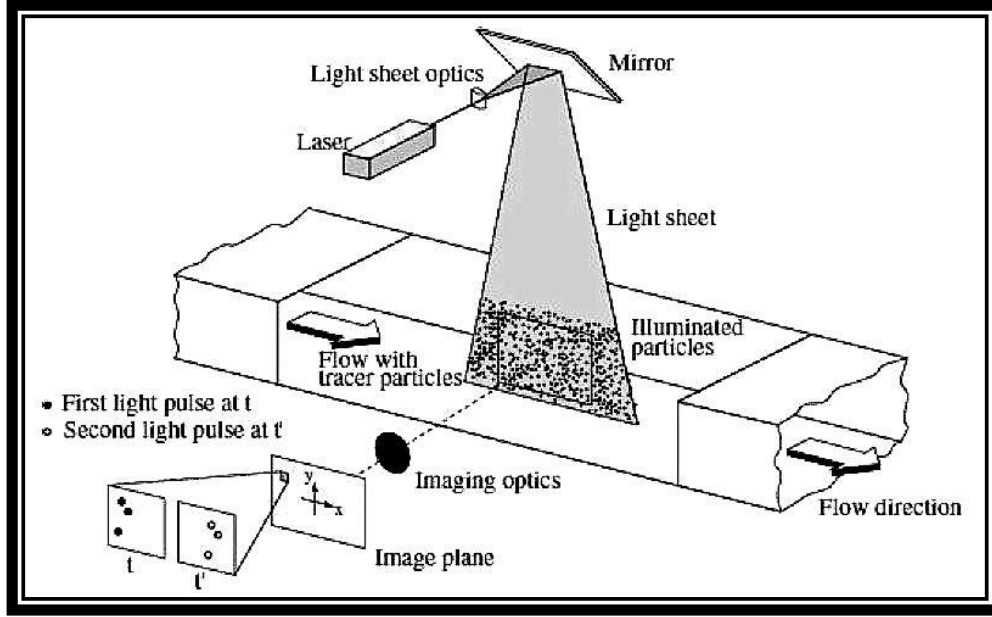


Figure 2.5: General PIV setup [16]

Figure 2.5 shows how data is obtained from using a PIV setup. As shown in the figure, the laser is fired into an optical component which changes the beam from its original Gaussian distributed beam, to a light sheet. This sheet then illuminates the particles in the flow, which are then recorded with the CCD camera, and finally post processed using an image processing technique or software. It is to be noted however, that the light sheet generated is not completely 2-dimensional, but the image capture is. The light sheet is not a sheet, but a volumetric space which can be reduced by using the right optics, and distancing all equipment appropriately. It is because of this that the image must be focused in the mid plane inside the light sheet volume where the laser intensity is highest.

### 2.3.2 PLANAR LASER INDUCED FLUORESCENCE (PLIF)

The works of Grisch and Orain [17] show a general overview of laser induced fluorescence (LIF). The main principle behind LIF is the use of pulsed laser energy to increase the energy in combustion species such that they reach what is referred to as the excited state. Once the molecule

reaches this excited state, then it will begin to emit radiation energy causing it to fluoresce until it then reaches a state of decay. Figure 2.6 shows a clear representation of what happens when a particle absorbs enough energy from the laser.

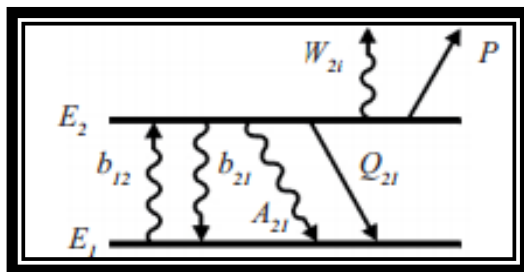


Figure 2.6: Visual representation of molecular activity after energy absorption [17]

This allows the image capture of the molecule using a CCD camera and intensifier. The fluorescence is captured at specific wavelengths according to different species as seen in Table 2.2. These wavelengths provide information on what frequency the pulse laser should be fired to cause the fluorescence of individual molecules. A band pass filter is used to isolate the image capture to a specific wavelength and eliminate any imaging caused by chemiluminescence. The most commonly analyzed combustion radicals are OH, CH, and  $\text{CH}_2\text{O}$ . These molecules can be used to define the flame front in different ways. OH is the most abundant radical present, and it also offers the most intense image capture [18]. Most studies using OH-PLIF imaging are successful, and this molecule is heavily favored when conducting LIF experiments. One limitation to analyzing OH is the fact that this radical is not a clear indicator of the exact flame front position, or flame thickness. This is due to the fact that OH can generate high intensity fluorescence after the flame front.  $\text{CH}_2\text{O}$  (formaldehyde) is also be used to generate flame imaging, but similarly to OH,  $\text{CH}_2\text{O}$  can generate fluorescence outside of the flame front. The most precise method for imaging is using the CH radical. This radical occurs along the flame front, and thus can provide



an accurate measure of the flame front thickness if successful imaging is obtained as shown in Figure 2.7.

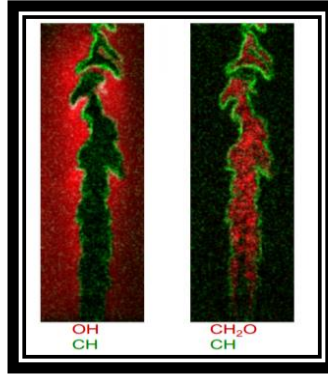


Figure 2.7: OH, CH, and CH<sub>2</sub>O imaging for a simple jet [19]

Dye Lasers are used due to their ability to be tuned to a broad range of wavelengths, particularly in the visible spectral range, the near ultraviolet and near infrared regions. This non-intrusive optical technique, like the PIV, resolves important information about the structure of the flame and the combustion process for the next generation combustor design. This type of laser system can be used to gather experimental combustion data which can be used to validate turbulent modeling.

Table 2.2: Absorption wavelengths for different combustion species

Molecule	Absorption wavelength (nm)
OH	306
C <sub>2</sub>	516
CH	431
CH <sub>2</sub> O	320-360
NO <sub>2</sub>	450-470

Appendix II shows the specifications of the LIF system and intensifier used for this project.

## 2.4 Flame Regimes

Flame characteristics change in accordance to the fluid conditions during combustion. There are various methods and theories explaining these characteristics, but a widely used method for classifying these different types of flames, was proposed by Borghi, and later modified by Peters [20-21], and is known as flame regime diagram (Figure 2.8). The diagram is characterized by dimensionless parameters ( $Re_T$ ,  $Da$ ,  $Ka$ ), turbulent parameters ( $u'$ ,  $L_T$ ), and flame parameters ( $S_L$ ,  $\delta_L$ ). Figure 2.9 shows theoretical pictorial representations of these flame regimes, and how the flame fronts are affected.

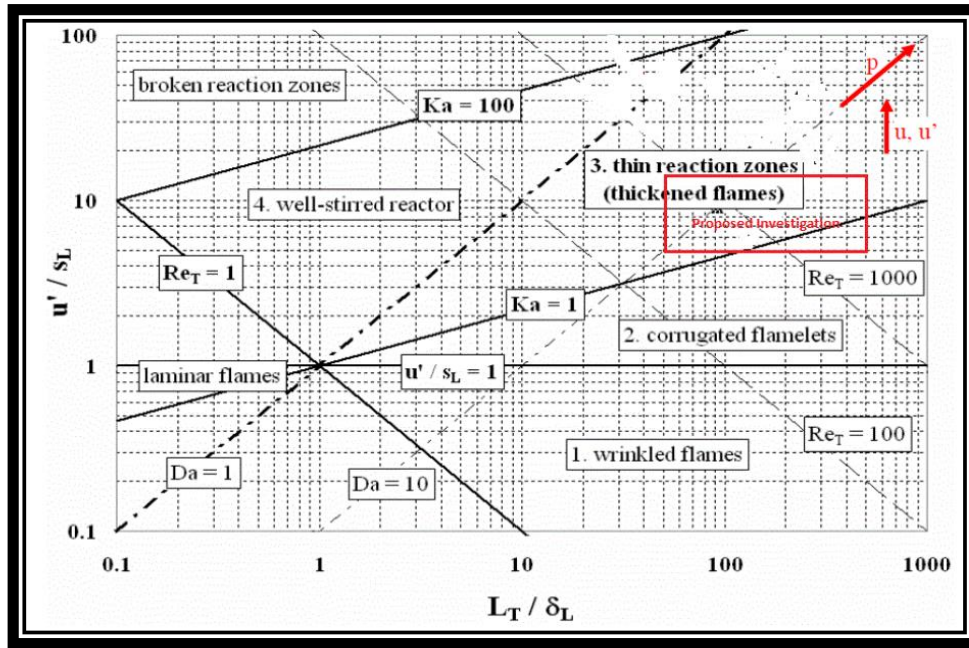


Figure 2.8: Flame regime diagram by Borghi and modified by Peter

The different flame regimes are explained in order to clarify the flame front behavior at varying turbulence. The region of interest in this project is the thin reaction zone which causes a thickened flame. This flame regime was proposed and studied by Zimont [22], and has been studied extensively in order to understand turbulent mechanics in combustion. This flame regime can be seen in application where turbulence is a determining factor in design such as in turbines, ramjet, and scramjet engines.





flame regime	$Re_T$	$Da$	$Ka$	$u'/s_L$	$\delta_L/\eta$	graphical illustration of the flame front
wrinkled flame	$> 1$	$> 1$	$< 1$	$< 1$	$< 1$	
corrugated flame	$> 1$	$> 1$	$< 1$	$> 1$	$< 1$	
thickened flame (thin reaction zones)	$\gg 1$	$\geq 1$	$> 1$	$\gg 1$	$> 1$	
distributed flame (well-stirred reactor)	$> 1$	$< 1$	$> 1$	$> 1$	$> 1$	

Figure 2.9: Different flame regimes and the graphical illustrations of flame front characteristics

### Wrinkled Flame Regime

The wrinkled flame regime occurs when flame speed is higher than the fluctuations in the flow field, and thus the combustion kinetics have a higher effect on the flame front. The flame thickness is smaller than the integral length scale, meaning the flow eddies are much larger than the flame thickness and therefore cause a turbulent appearance in the flame, hence the wrinkled flame.

### Corrugated Flame Regime

The corrugated flame occurs when turbulent intensity predominates over flame speed, thus causing breakup in the flame front. Breakup occurs due to the fact that  $Ka < 1$ , therefore the flame thickness is still smaller than the small scales in the turbulent flow. This cause the flame to exhibit vortices in its flame front which can cause pockets of unburnt reactants to be present in the flame.

### Thickened Flame Regime

The thickened flame occurs when the turbulent intensity is much greater than the flame speed, causing higher levels of disruption in the flame front than in the previously discussed corrugated flame. The increase in turbulence also causes the small scale eddies to be smaller than

the flame thickness. This in turn causes the small scale eddies to enter the flame reaction zone and cause a thickened flame front. The flame is also stretched and the reaction zone is altered when the flame is thickened such that the flame speed can increase due to the inner reaction zones within the flame front. This present study system aims to achieve the conditions required to generate a thickened flame experimentally. In this work, the author focuses on the quantification of the turbulent parameters  $u'$  and  $L_T$ , which will be used with future LIF data to determine the thickened flame characteristics.

### **Distributed Flame Regime**

This flame regime occurs when the chemical kinetics of the combustion controls the combustion process. A distributed flame is achieved when the mixing of the reactants is higher than the time scales during combustion. This causes a flame which is evenly distributed, and whose flame front is unlike any of the previously mentioned flames.

## Chapter 3: Experimental Setup

### 3.1 System description

The design of this turbulent combustion system has been discussed previously [5]. As previously mentioned, the current system is to be operated with air and methane as reactants in order to study combustion at compressible flow rates ( $M > .3$ ). The system requirements which drove the design of this system can be seen in Table 3.1. The main combustor is shown in Figure 3.1, and consists of the following; combustion chamber, entrance and exhaust regions, mixing chamber, quartz windows, and modular backward-facing step. The other subsystems are discussed in detail in the following sections to provide an understanding behind the overall design of the high turbulent intensity system.

Table 3.1 System Requirements

System	Requirement
Combustion chamber	Optically accessible
	Grid turbulence generator
	Changeable step size (variable dimension)
	Max Pressure: 6 bar ( 87 psi)
Reactants	Air / CH <sub>4</sub>
Air	Pre-heated at 400-600 K (260 – 620 F)
	Velocity Mach $> 0.3$
	Flow rate: Max at 0.4 kg/s
CH <sub>4</sub>	Flow rate: Variable (max 0.07 kg/s)
Inlet pressures	100 - 600 kPa (14 - 87 psi)
$U'/S_L$	5-10
$L_T/\delta$	50-200

An exploded model of this subsystem can be seen in Figure 3.1, and a cross-sectional model showing the assembled chamber is shown in Figure 3.2. The design of the entrance and exhaust regions is based on a polynomial profile curve which allows for the entrance and exhaust the combustor to follow a uniform ‘top hat’ velocity profile [23]. Extensive FEA and CFD modeling has been performed on this subsystem to validate the design and ensure it can meet the system

requirements, while also maintaining the safety of those operating it. The FEA analyses were conducted under maximum chamber pressure of 6 bar and maximum temperature of 500K. Table 3.2 shows the subsystem components and their respective factor of safety (FOS). This table shows that the failure mode will occur at the windows; more specifically the top window. In order to address this, the thermal expansion is considered when choosing a gasket for the combustor windows and flanged unions. The chosen gasket material is a homogenous high temperature application graphite gasket sheet. This gasket material can withstand up to 6000K at pressure of 10 bar, which is well above the maximum conditions the system will operate at. This gasket material also has a 40% compression ratio with 20% recovery factor, which offers the desired dimensions once thermal expansion is considered along the largest stainless steel to quartz interface. A perforated plate is used as a turbulator in order to cause grid induced turbulence as described in Chapter 2. The three different grids consist of a rectangular plate with a 5x5 array of holes. The different grid blockage ratios are 54%, 61%, and 67%. The placing of this grid is shown in Figure 3.2.

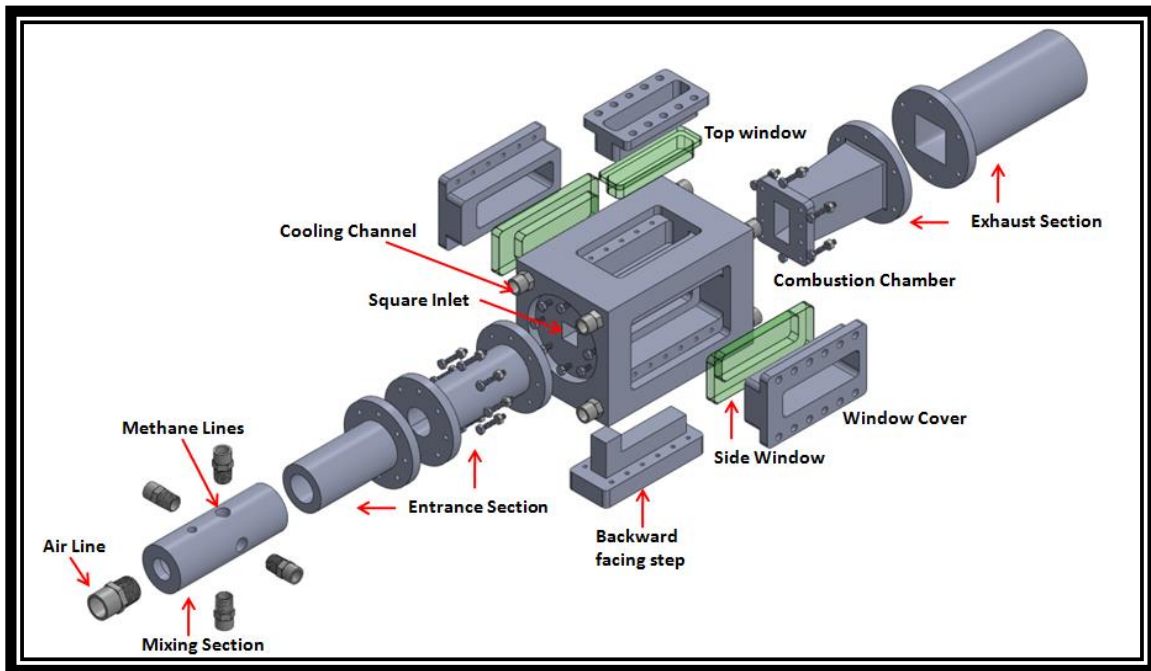


Figure 3.1: Exploded model of the combustor subsystem and its components

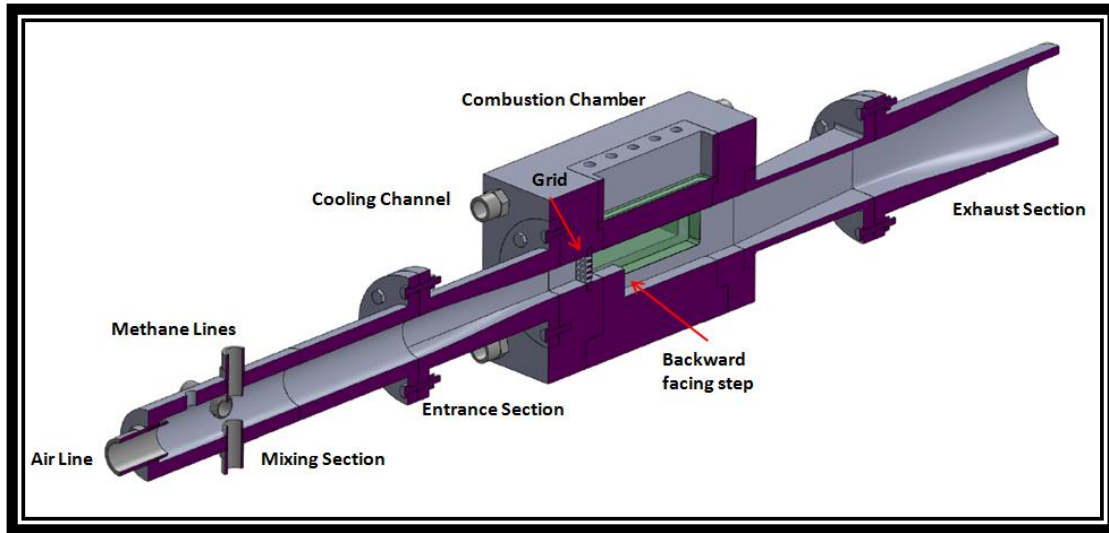


Figure 3.2: Cross-sectional view of the combustor showing 2D plane used in simulations [5]

Table 3.2: Components in combustor and their factor of safety

Component	FOS
Window (thinnest)	3.5
Entrance/Exhaust section	11.8
Grid	16.8
Combustor	12

The main air line consists of 1” 316 Stainless Steel tubing which draws air from a compressor that can operate at 190 scfm and 140 psig. This flow rate allows the experiments to be conducted at compressible air conditions. The line is insulated after the preheating section to prevent temperature drop of the preheated air. Sizing, pressure, density, and Mach number calculations were carried out using compressible flow theory [24]. An overall schematic of the system can be seen in Figure 3.3. Figure 3.4 and Figure 3.5 show the pilot flame subsystem, which will serve as the ignition source for the flame in the combustor, in greater detail. This pilot flame subsystem will operate using two hydrogen-air premixed flames integrated into the modular step.

The image contains two detailed process flow diagrams for a combustion system, labeled 'Experimental Schematic' and 'Pilot flame schematic'.

**Experimental Schematic:** This diagram shows the main experimental setup. It includes a Laboratory Water Supply, Laboratory Compressed Air Supply, and Laboratory Exhaust. The system features a 1" Cu Tubing network, a 1/4" Orifice, a Combustion Chamber (with TC-04 and PT-03 sensors), a Mixing Chamber, and a Particle Seeder. A Pilot Flame Subsystem is connected to the Combustion Chamber. The system also includes a Heater, a 1 1/2" Steel Pipe, and a 1/2" SS Tubing network. Various valves (SV-01 to SV-10), pumps (PU-01, PU-02), and pressure transducers (PT-01, PT-02) are shown. A K-bottle (Compressed Air, 140 psig) and a Compressor (located in ENGR Bldg basement, x3 Accumulators) are also depicted.

**Pilot flame schematic:** This diagram shows a simplified version of the experimental setup, focusing on the pilot flame. It includes a Laboratory Water Supply, Laboratory Compressed Air Supply, and Laboratory Exhaust. The system features a 1" Cu Tubing network, a 1/4" Orifice, a Combustion Chamber (with TC-04 and PT-03 sensors), a Mixing Chamber, and a Particle Seeder. A Pilot Flame Subsystem is connected to the Combustion Chamber. The system also includes a Heater, a 1 1/2" Steel Pipe, and a 1/2" SS Tubing network. Various valves (SV-01 to SV-10), pumps (PU-01, PU-02), and pressure transducers (PT-01, PT-02) are shown. A K-bottle (Compressed Air, 140 psig) and a Compressor (located in ENGR Bldg basement, x3 Accumulators) are also depicted.

**LEGEND:**

Symbol	Description
[K-bottle symbol]	Gas K-bottle
[Accumulator symbol]	Accumulator
[Compressor symbol]	Compressor
[Pressure Regulator symbol]	Pressure Regulator
[1/4 Turn Valve symbol]	1/4 Turn Valve
[Solenoid Valve symbol]	Solenoid Valve
[Relief Valve symbol]	Relief Valve
[Pressure Transducer symbol]	Pressure Transducer
[Thermocouple symbol]	Thermocouple
[Flow Controller symbol]	Flow Controller
[Check Valve symbol]	Check Valve
[Radiator symbol]	Radiator
[Pump symbol]	Pump
[Orifice symbol]	Orifice
[Direct-contact heat exchanger symbol]	Direct-contact heat exchanger
[Humidity Filter symbol]	Humidity Filter
[Tubing symbol]	Tubing
[Insulated Tubing symbol]	Insulated Tubing
[Gas Flow symbol]	Gas Flow
[Cold Dynalene Flow symbol]	Cold Dynalene Flow
[Hot Dynalene Flow symbol]	Hot Dynalene Flow
[Water Flow symbol]	Water Flow

19



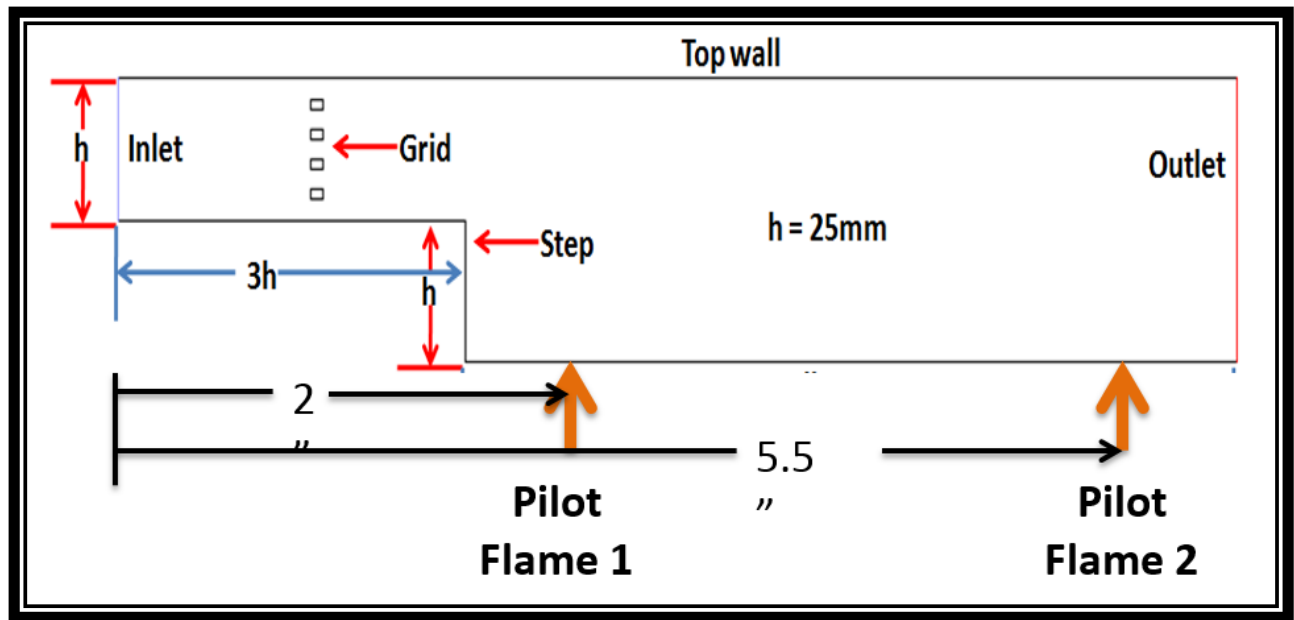


Figure 3.4: Combustion chamber showing location of pilot flames

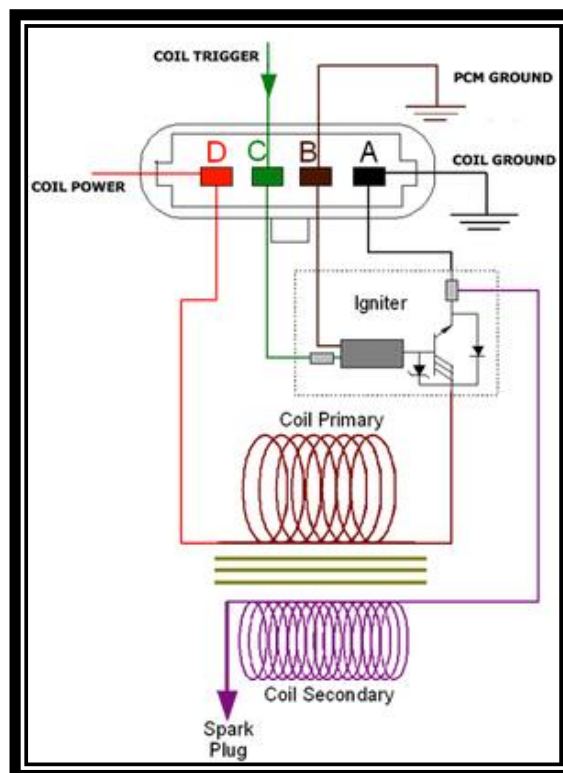


Figure 3.5: LS1 coil wiring diagram

### 3.2 Air Preheating

To preheat the air to the desired maximum 500K temperature, a large heat source is to be considered. The constraints for determining the preheating section were based on the main laboratory constraint of having 100A of current with a 3-phase, 480V source. The most effective way to utilize the electrical power to heat the air is through the use of a resistance heater with high efficiency. A 100kW commercial heater with a 10% efficiency will be used to preheat the air. Figure 3.6 shows a schematic of this heater, and Figure 3.7 shows the heating elements encased within the heating unit. The required heat vs the maximum heat that can be obtained was first compared in order to ensure the possibility of preheating the air to the required temperature. This was done via a simple energy calculation required for the air and maximum electrical power available.

$$\dot{Q} = \dot{m} * c_p * (T_h - T_L) \quad (3.1)$$

$$P = 0.9 * I * V * PF * \cos(\phi) \quad (3.2)$$

Where the air properties are based on maximum conditions, V, PF, and  $\phi$  are the voltage, power factor (0.95 for resistance heaters), and phase respectively. These calculations show the power delivered by the heater is sufficient to preheat the air at maximum conditions.

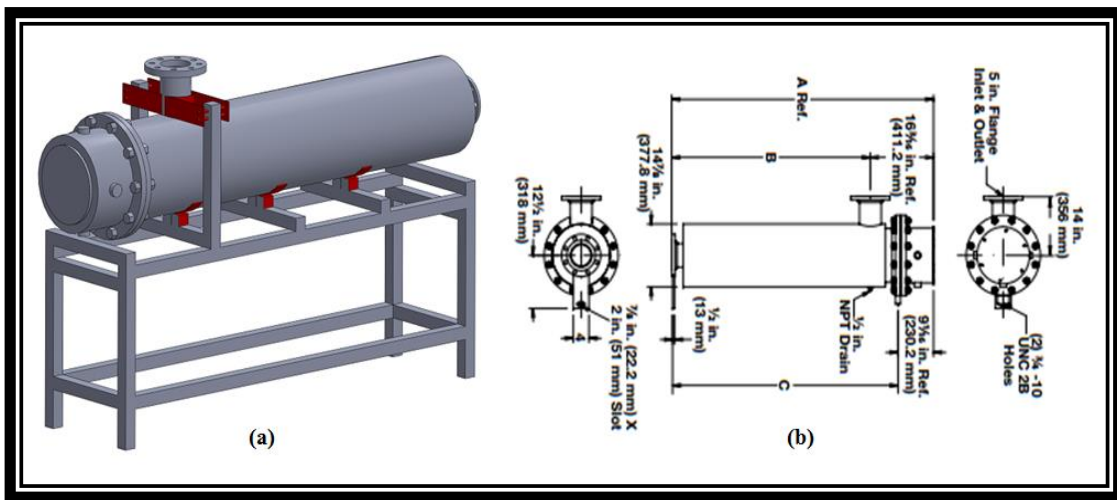


Figure 3.6: Heater (a) model with stand and (b) manufacturer specific drawing

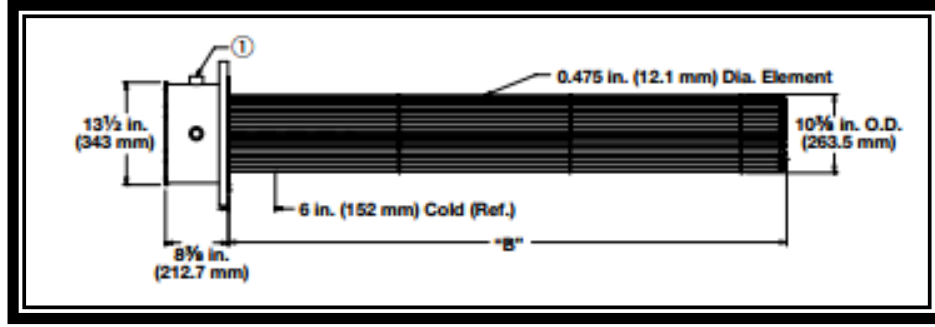


Figure 3.7: Inconel heating elements inside the heater

The heating elements consist of 36 hairpin Inconel elements with a heat flux of  $3.6 \text{ W/cm}^2$ . Using this information and assuming convective heat transfer between the air and heating elements, we can find a value for the exit temperature of the air.

$$T_{air,out} = T_{in} + \frac{\dot{q}A_s}{\dot{m}c_p} \quad (3.3)$$

The exit temperature of the air is 515K, which gives a 15 degree margin for the preheated air. The theoretical value was then validated by carrying out a computational model using the full scale dimensions, material, and flow properties. A transient k- $\epsilon$  turbulent model was used in ANSYS 14.5 Academic version with a 2D mesh consisting of a 400000 structured elements biased toward the exit section of the heater. Viscous heating was enabled, and second order upwind solutions were obtained. The transient solution is carried out for 5 minutes, then 10 minutes in order to extract a steady state temperature profile. Figure 3.8 shows the time resolved solution, concentrated at the exit region of the heater and its temperature contours. Figure 3.9 shows a plot extracted from the two transient solutions, assuming that after 10 minutes the flow is considered steady state. Table 3.3 shows a comparison between the theoretical and calculated values of exit temperature. It should also be noted that after the preheating section the air, though insulated, will lose  $\sim 10\text{K}$  due to compressible flow effects. Appendix III shows the compressible flow equations including Fanno-line flow (assuming isothermal flow) used to calculate these effects.

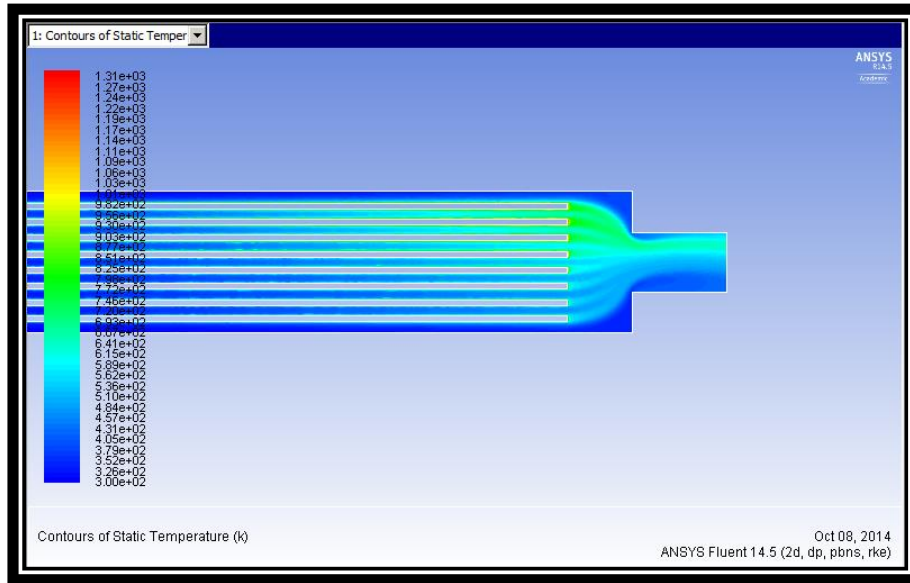


Figure 3.8: Static temperature contours of preheated air

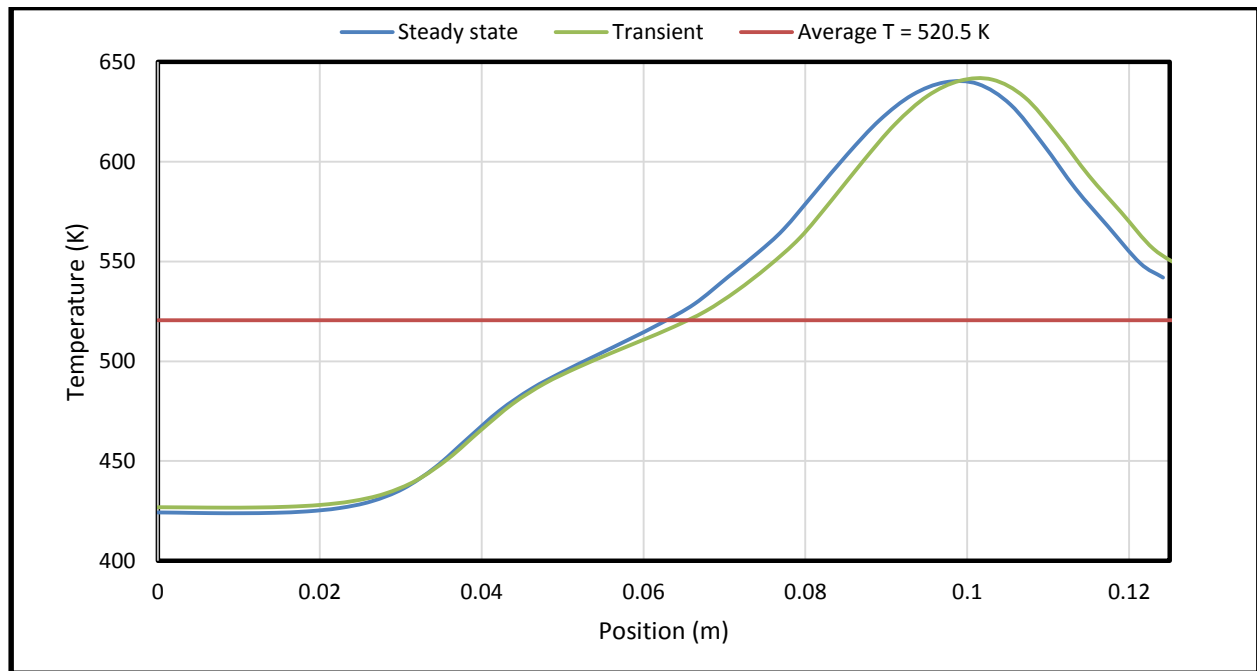


Figure 3.9: Plot of steady state, transient, and average temperature profiles at heater exit

### 3.3 Exhaust Design

The exhaust design was developed to meet the temperature requirement of exhaust gases not exceeding temperatures of 80 °C. The exhaust fan inside the laboratory has a suction capability of 230 scfm, which is above our maximum operating conditions. The exhaust temperature of the air is assumed to be 800K at maximum operating conditions based on preliminary combustion modeling [5]. Several methods for exhaust cooling were proposed including the use of a coolant similar to the combustor cooling, and liquid nitrogen spraying to reduce the exhaust gas temperature. These methods however required a more intricate design and would be difficult to control in an automated sequence. The method used now consists of water spraying inside a non-oxidizing tank which acts as a heat exchanger. The water is sprayed with the use of a commercially available nozzle, with a 90° full cone spray angle. Initially the use of three spray nozzles (Figure 3.10) was employed to decrease the modes of failure in the subsystem, but ultimately the redundancy was eliminated and only one nozzle is used. The water supplied by the water connections in the laboratory fluctuates from 15 – 20 gallons per minute (gpm), and the water pressure is 70 psi. The spray nozzle is design to supply 13 gpm of water at a supply pressure of 70 psi, and consists of a 0.31” orifice diameter.

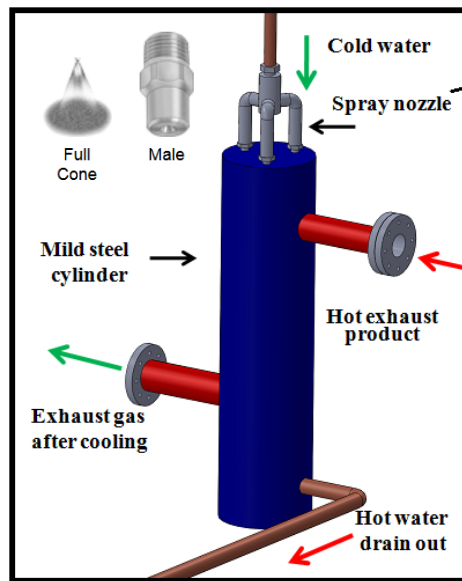


Figure 3.10: Initial conceptual model of exhaust section with spray nozzle diagram

The analysis for the exhaust cooling was done both theoretically and computationally, employing equations of heat transfer, and a multi-phase model. In order to find the amount of water needed, a system of equations is used and includes the mass fraction of liquid water and steam. The equations are solved using the properties of water and steam, as well as the initial temperature of 800K such that-

$$\dot{Q}_{exhaust} = \dot{Q}_{water} + \dot{Q}_{steam} \quad (3.4)$$

$$(\dot{m}c_p(T_{h2} - T_o))_{exhaust} = (\dot{m}_{liquid}c_p(T_o - T_{water}))_{water} + (\dot{m}c_p(T_{vapor} - T_{water}) + \dot{m}h)_{steam} \quad (3.5)$$

$$\dot{m}_{water} = \dot{m}_{liquid} + \dot{m}_{steam} \quad (3.6)$$

The computational model used the result of the mass of water from the previous equations at a temperature of 293K, and pressure of 70 psi. The total mass of the products of combustion at 800K and ambient pressure is used. A transient, multi-phase turbulent k-ε model was used to carry out the simulation with dimension of the spray nozzle and water tank as specified by the manufacturer. The model was run using ANSYS 14.1 Academic version with a total of 200000 elements. The results are shown in Figure 3.11, and the results of the computational temperature compared to the theoretical value are presented in Table 3.3. The minimum water flow rate required to cool the exhaust gas is 7.5 gpm, which is less than the maximum flow provided by the spray nozzle. A pump is used in order to drain the accumulated water out of the tank at a flow rate higher than the nozzle. A supplementary dilution line was also added to the exhaust in case an unburned mixture entered the exhaust.

Table 3.3: Comparison between theoretical and CFD results

Theoretical exhaust temperature	CFD mean temperature
333K	340K

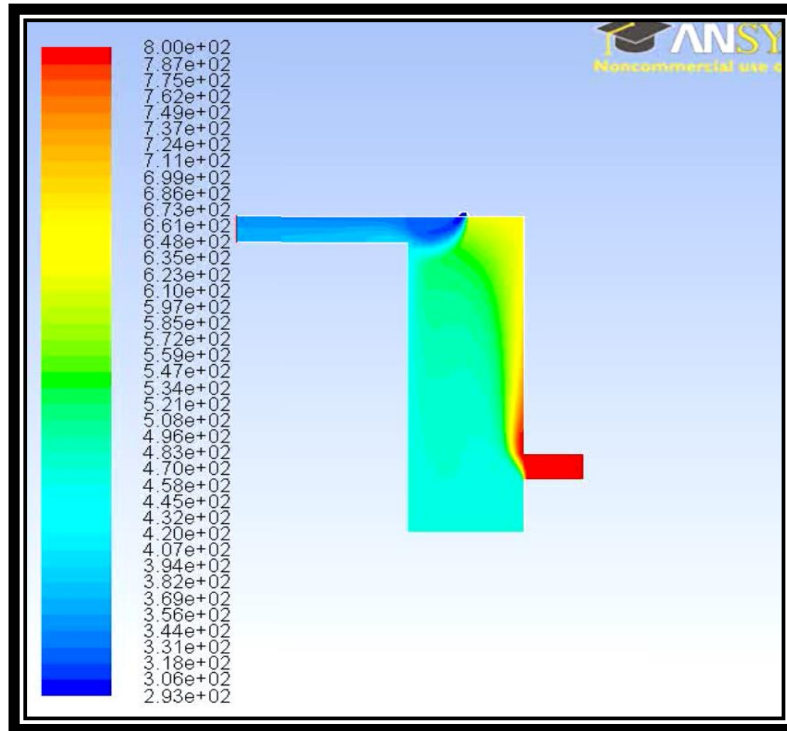


Figure 3.11: Temperature contours in exhaust simulation

### 3.4 Combustion Chamber Cooling

As temperature rises inside the combustor during combustion, the structural integrity of the combustor subsystem is compromised, and running time becomes an important issue. The use of various cooling methods were taken into consideration, but a pre-existing heat exchanger was rerouted to flow coolant through the combustor. Figure 3.12 illustrates the conceptual and actual setup of the heat exchanger. Figure 3.13 shows additional information about the heat exchanger which can supply a cooling load of 200kW. In order to address the temperature rise within the combustor during the combustion process, cooling channels were manufactured into the combustor. These cooling channels are 9.5” long, have a 0.5” diameter and there are 4 channels in total. These channels will flow dynalene HC-10, a non-toxic coolant, at a rate of 5.6 – 10 gpm. The properties of this coolant are obtained from the manufacturer [25]. The temperature at different

critical points in the combustor was calculated using equations for transient heat transfer on a convective surface [26]. These calculations are used with the log mean temperature difference method (LMTD) calculations associated with the coolant flow inside the combustor channels.

$$\dot{q}_s(t) = h[T_\infty - T(0, t)] \quad (3.7)$$

$$\frac{T(x, t) - T_i}{T_\infty - T_i} = \operatorname{erfc}\left(\frac{x}{2\sqrt{\alpha t}}\right) - \exp\left(\frac{hx}{k} + \frac{h^2 \alpha t}{k^2}\right) \operatorname{erfc}\left(\frac{x}{2\sqrt{\alpha t}} + \frac{h\sqrt{\alpha t}}{k}\right) \quad (3.8)$$

$$\Delta T_{ln} = \frac{\Delta T_e - \Delta T_i}{\ln\left(\frac{\Delta T_e}{\Delta T_i}\right)} \quad (3.9)$$

These equations were solved for different flow conditions inside the combustor and inside the cooling channels to find a relationship between the coolant and the temperature at certain thicknesses of the combustor walls. Equation 3.8 is also applied to the quartz windows in order to calculate the difference in thermal expansion of the stainless steel and quartz interfaces [27].

$$\frac{\Delta L}{L_o} = \alpha \Delta T ; \quad \frac{\Delta A}{A_o} = 2\alpha \Delta T ; \quad \frac{\Delta V}{V_o} = 3\alpha \Delta T \quad (3.10)$$

Comparing the thermal expansion differences using the temperatures from Figure 3.14, the adequate gasket sizing was chosen to be 1/16” thickness.

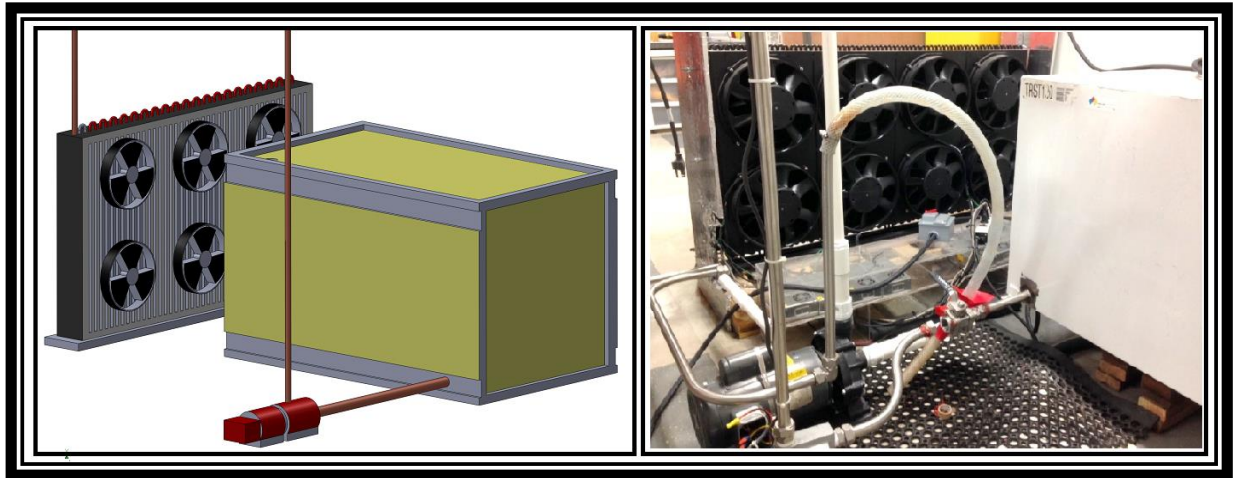


Figure 3.12: CAD model of heat exchanger and dynalene tank (left) and physical setup (right)



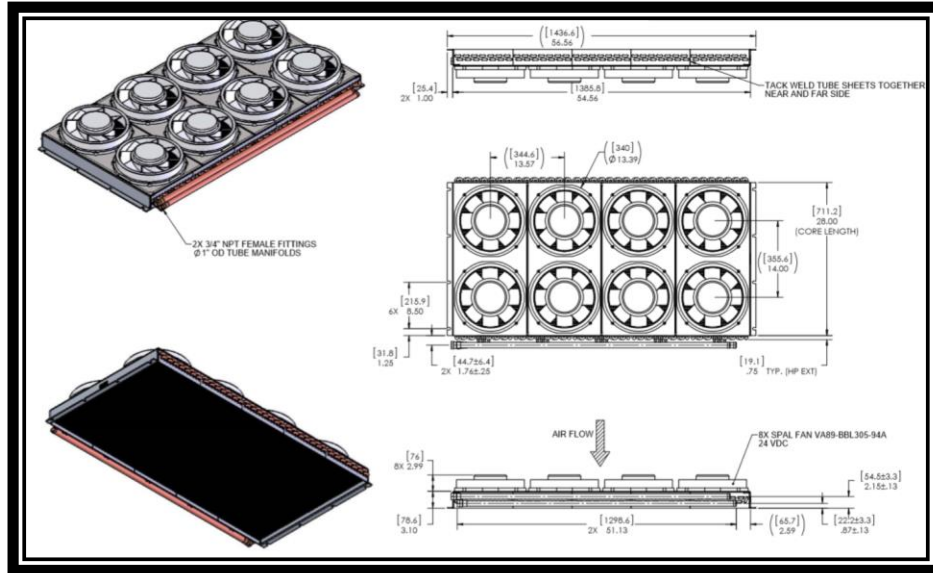


Figure 3.13: Additional schematic of heat exchanger used for cooling

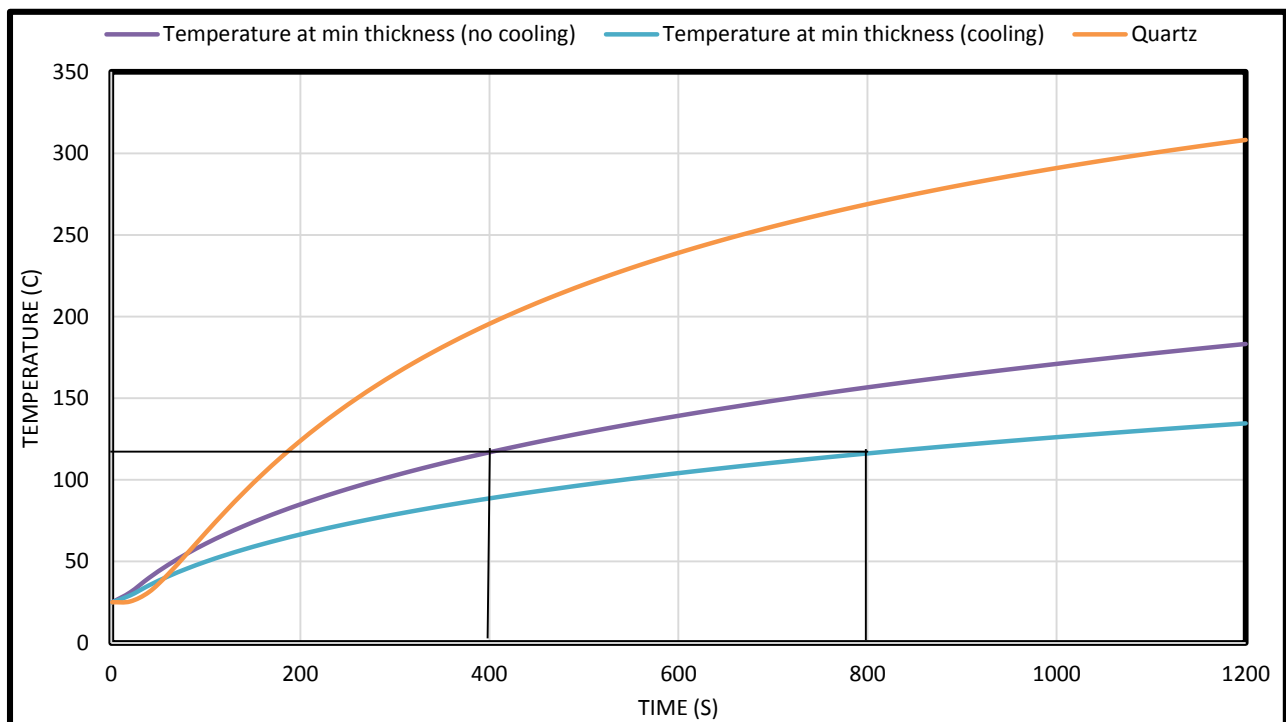


Figure 3.14: Temperature vs time plots for critical thickness and largest quartz window

Using the thermal expansion of stainless steel and quartz with Figure 3.14, the determined allowable temperature is 125 °C. The allowable run time is doubled when the combustor is being cooled with the dynalene.

### 3.5 Control System

The control system setup was designed with two objectives in mind; to be able to control all the instrumentation manually as well as automatically through the use of LabVIEW with National Instruments PCI cards, and to be efficient and simple to operate. In order to achieve this, all instrumentation was wired into a single space consisting of:

- Main control box with connector blocks attached which controls:
  - o AC valves
  - o DC valves
  - o Manual emergency stops
  - o Spark plug ignition
- DC power supplies for valves and instrumentation (thermocouples, transducers)
- LabVIEW designated CPU for running automated sequences
- Signal generator for pilot flame ignition

This control box is shown in Figure 3.15 and the corresponding electrical schematic is shown in Figure 3.16. There are two separate manual emergency stops in the control system; one for all gas controlling valves, and one for water controlling valves. The control box also consists of a double pole-double throw (DPDT) switch which serves as a manual override in case of a CPU or software malfunction. The LabVIEW program consists of four Data Acquisition assists to accommodate for the different signal each type of instrumentation requires. Table 3.4 presents what each DAQ assist controls. The LabVIEW interface block diagrams are shown in Figure 3.17 and 3.18 respectively.

Table 3.4: DAC controlled instrumentation

DAQ Assist	Instrumentation controlled/monitored
1	Pressure transducers, flowmeters, and thermocouples
2	Air/methane line valves
3	Air and methane proportional control valves
4	Pilot flame valves



Figure 3.15: Main control box

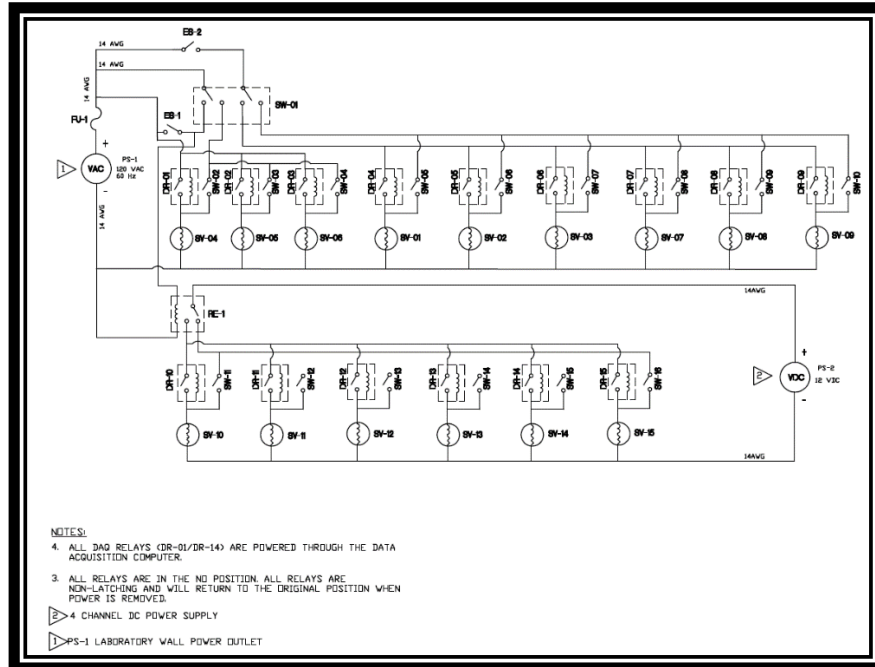


Figure 3.16: Electrical schematic of main control box

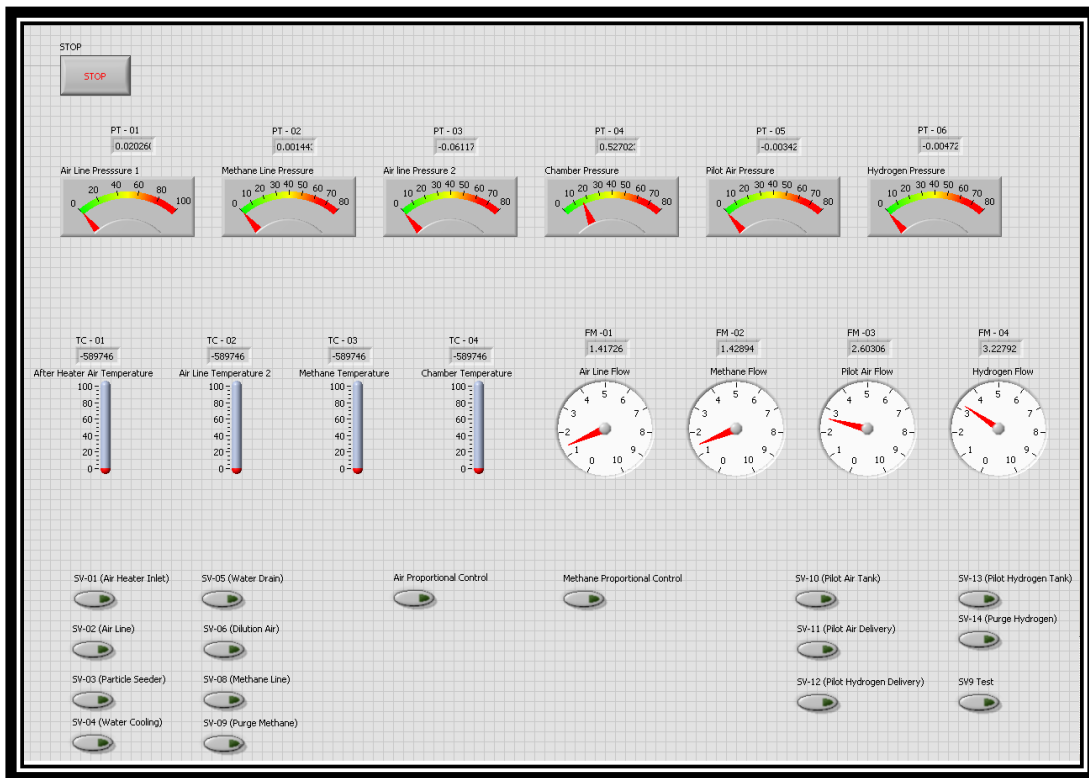


Figure 3.17: LabVIEW control panel interface

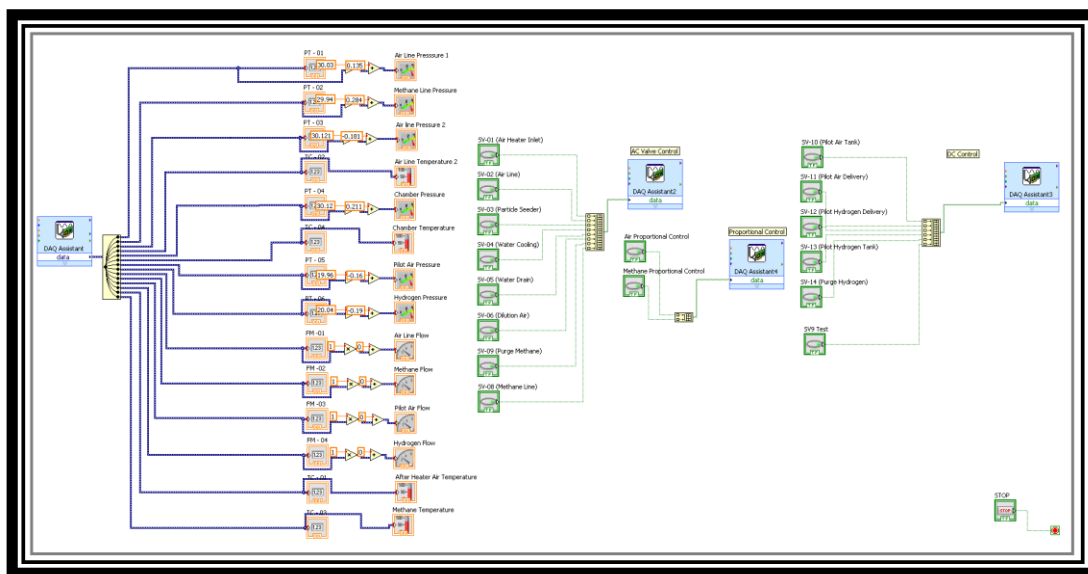


Figure 3.18: DAQ assist block diagram

### 3.7 Test Setup Summary

To summarize, the system can be described using Table 3.5. The subsystems and their function are explained. For the present work however, only the main air, exhaust, and PIV subsystems are considered.

Table 3.5: A summarization of the subsystems that make up the high turbulent intensity system

Subsystem	Function
Combustor	Provides optical access in order to employ flow diagnostic techniques and study the previously mentioned research topics
Main air line	Provides cold/preheated air to the combustor for premixed flame combustion
Pilot flame	Ignition source for the air and methane reactants inside the combustion chamber
Methane line	Provides methane to the combustor for premixed flame combustion
Exhaust	An exhaust which serves as an escape which cools the hot combustion products to a safe and acceptable temperature
Chamber cooling	Cools the combustor in order to prolong combustion run time for up to 13 minutes
Control system	Provides manual and automatic control of system instrumentation
PIV system	Laser diagnostics system used in the present work to characterize the turbulence scales of air at compressible conditions
PLIF system	Laser diagnostics system that allows the analysis of flame front characteristics.

## Chapter 4: Methodology

The present work focuses on the study of turbulent structures in the flow field at compressible air flow. Figure 4.1 shows the schematic pertaining to the setup used for the current work. A test matrix is developed to test the three different blockage ratios and volumetric flow rates as seen in Table 4.1. Before the tests are conducted, the PIV laser and CCD camera are synchronized and calibrated in order to optimize results. All data acquisition is obtained and post-processed using the ‘DynamicStudios’ software. The three different grids used are described in Table 4.2.

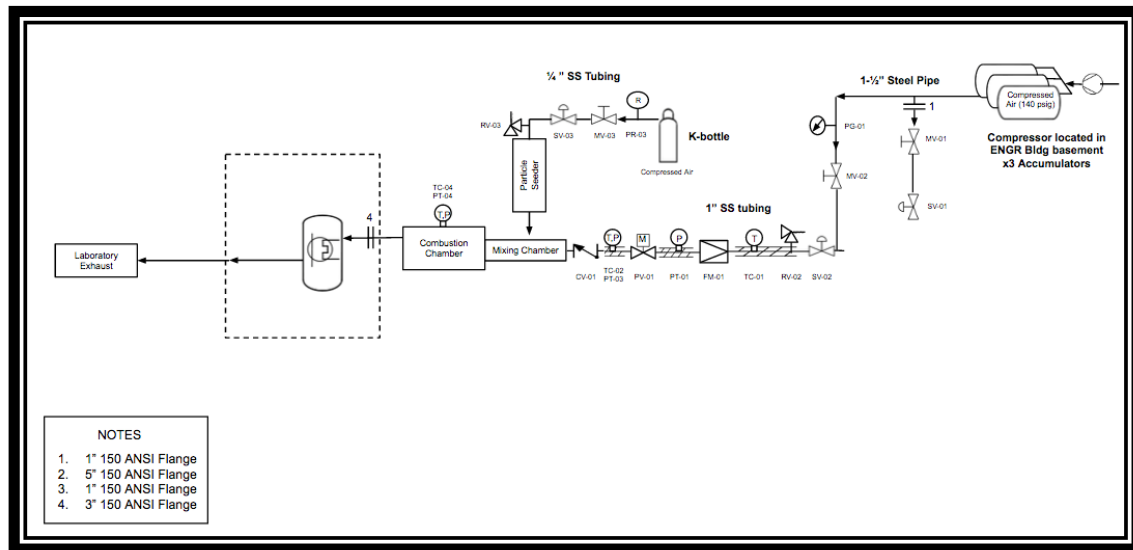


Figure 4.1: Flow schematic of the present study

Table 4.1: Test matrix for fluid flow studies

Blockage Ratio (%)	Fluid Temperature (K)	Test Pressure (PSIG)	Flow Rate (scfm)	Re
<b>54</b>	298	0	25	5762
<b>54</b>	298	0	55	12676
<b>54</b>	298	0	115	26506
<b>61</b>	298	0	25	5307
<b>61</b>	298	0	55	11676
<b>61</b>	298	0	110	24413
<b>67</b>	298	0	25	4852
<b>67</b>	298	0	55	10675
<b>67</b>	298	0	115	22321

To carry out the PIV experiments, a '*15-1000 Dual power*' 527nm Neodymium-doped Yttrium Lithium Fluoride (Nd-YLF) laser with a pulse energy of 15mJ/pulse was used. Laser is redirected at  $45^\circ$  through a telescopic lens which then generates the light sheet used to illuminate the alumina particles seeded into the flow. The image plane was captured by a 'Speed sense 9070' CCD camera with a frame rate of 3.1 kHz. The image plane was defined by the area the camera captures which contains the laser sheet; this area is a 64mm x 40mm space. The flow field was seeded with  $1\mu\text{m}$  alumina particles, and these particles are seeded far upstream to where the introduction of particles does not affect the cross-flow development. The camera and the laser pulse are synchronized and controlled using a BNC 575-8 time box. The timer box uses BNC cables to synchronize the laser firing pulse and the camera trigger rate. The signals of both components are routed through the timer box which synchronizes them in the 'DynamicStudios' software. The image is calibrated in order to form a correlation between pixel values, and physical dimensions. The image is calibrated while the laser is firing and particles are present in the flow to optimize the camera focus. Ideally, the camera will be focused in the center of the light sheet to capture the highest laser intensity plane. Raw PIV images were taken at a rate of 3 kHz in a double frame capture mode, and a total number of 375 images were used for analysis. The image number is obtained from the time step defined in Chapter 2, section 2.2.1. A raw image used for image calibration is shown in Figure 4.2 and a raw image detailing the image characteristics is shown in Figure 4.3.

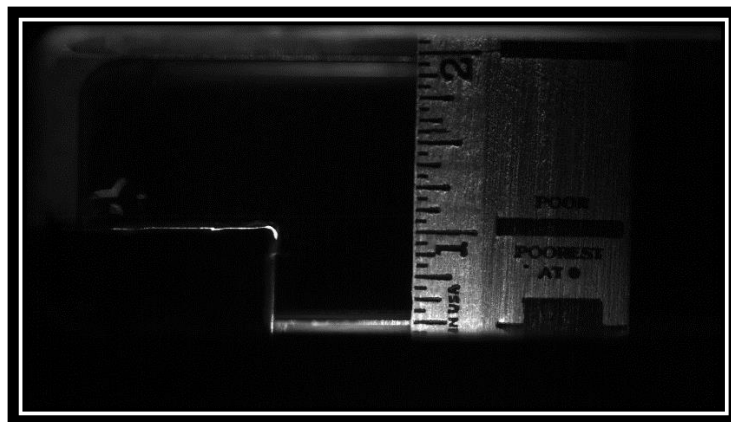


Figure 4.2: Raw PIV image showing calibration



Figure 4.3: Raw image detailing the different components in the PIV capture

The main air line is controlled by three different valves. A quarter turn manual control valve is used to allow air to enter the main airline into the system from the compressor mentioned in Chapter 3. The air passes through a 120 V (*AVCO E03/05 8P14*) solenoid valve which has a maximum torque of 35 Nm at 0.5 amp and a 12 second open/close time. After that the flow passes through a DC (*EZ 88E22-C0EWS-D01*) proportional control valve. The proportional control valve allows a 0 – 10V input signal to control how much the valve opens to allow air. The air passes through an analog flowmeter (*Hedland variable area flowmeter*) which has flow measurement range of 25 – 250 scfm at a pressure range of 40 – 120 psi and  $\pm 2\%$  accuracy. Figure 4.4 shows the solenoid valve, proportional control valve, and flowmeter. Figure 4.5 shows the laser system in operation. Figure 4.6 shows an overall view of the main air line and seeding point of alumina particles.



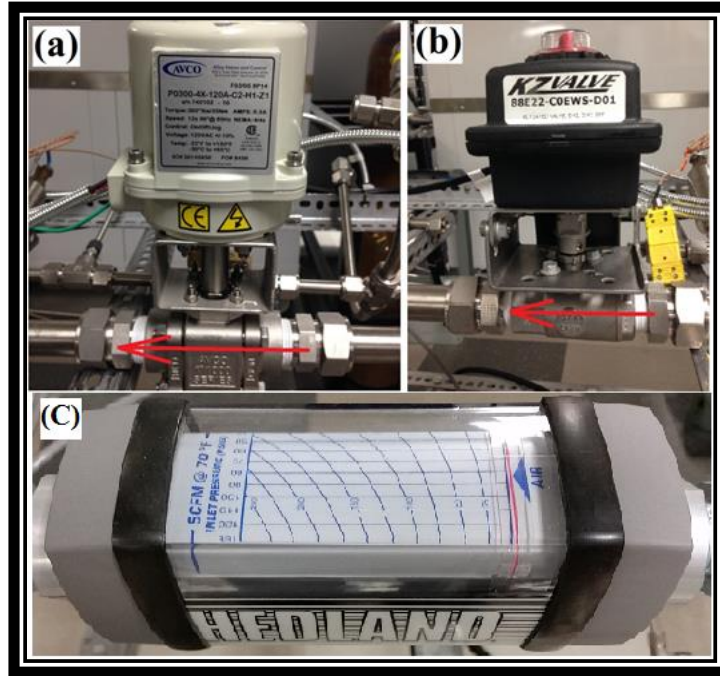


Figure 4.4: Solenoid valve (a), proportional control valve (b) and flowmeter (c)

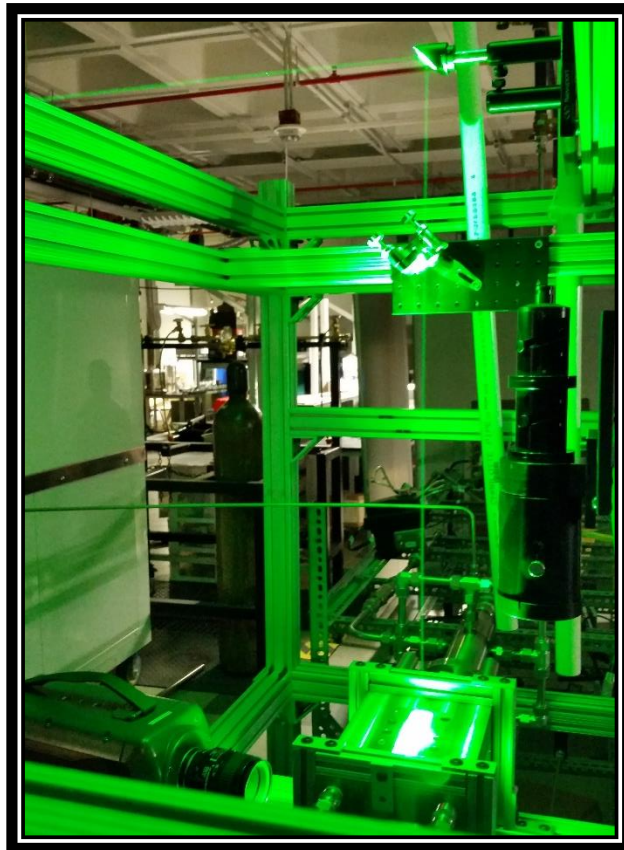


Figure 4.5: PIV system being fired into the combustor for flow analysis

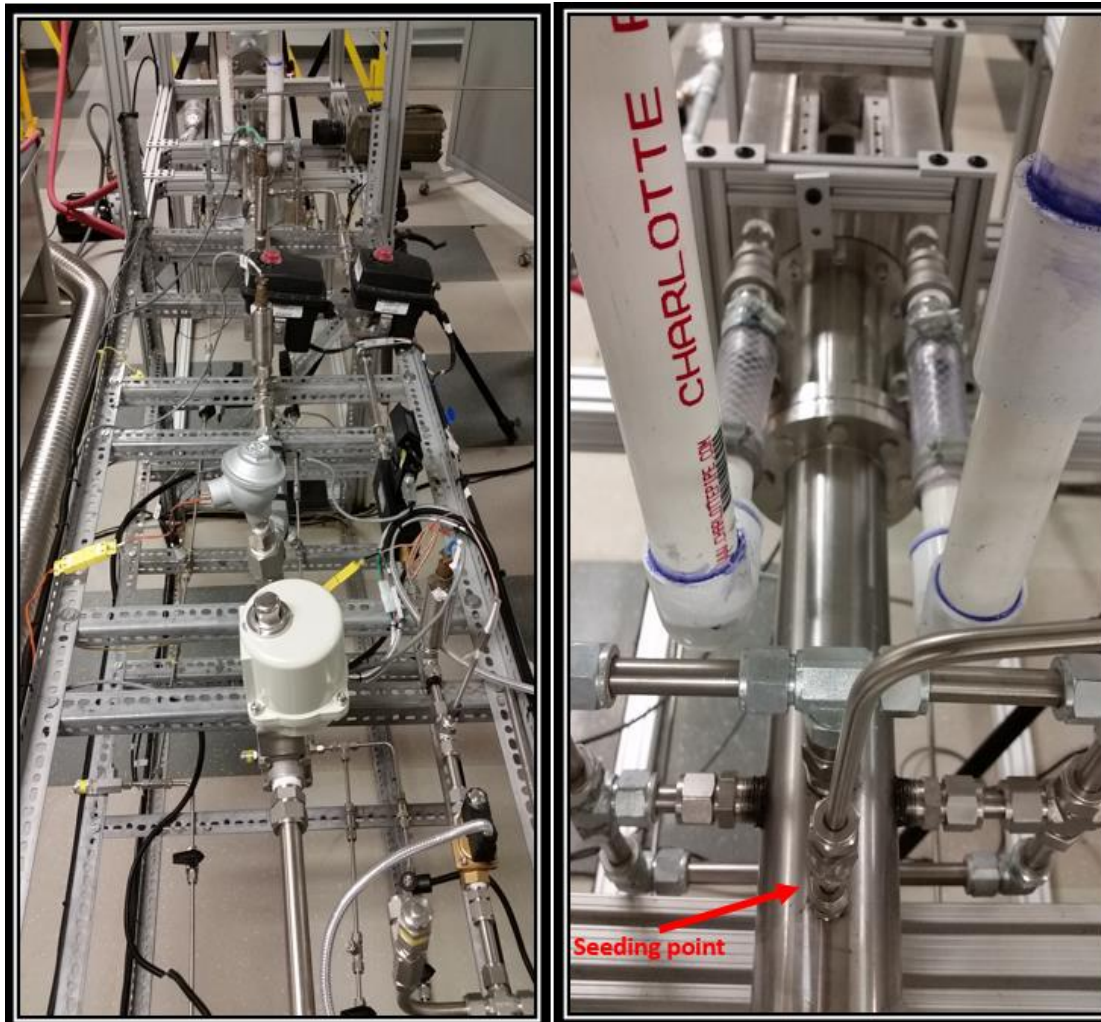


Figure 4.6: Main airline left and mixing chamber with seeding point indicated (right)

Table 4.2: Grid description

Blockage ratio (BR)	54%	61%	67%
Effective area (in <sup>2</sup> )	0.46	0.39	0.33
Hole area (in <sup>2</sup> )	0.0184	0.0156	0.0132
Hole diameter (in <sup>2</sup> )	0.153	0.140	0.129
Hole diameter (mm)	3.8	3.5	3.2

## Chapter 5: Result and Discussion

As previously mentioned, initial system validation has been conducted using PIV [28]. It was concluded that the flow field in the combustor exhibited the same behavior as seen in the LES simulations. The velocity profile showing agreement between the two methods, is shown in Figure 5.1. Additional testing was done in the present work to further validate the flow field.

Figure 5.2 shows an almost identical PIV image to that obtained in the LES model for  $Re = 815$ .

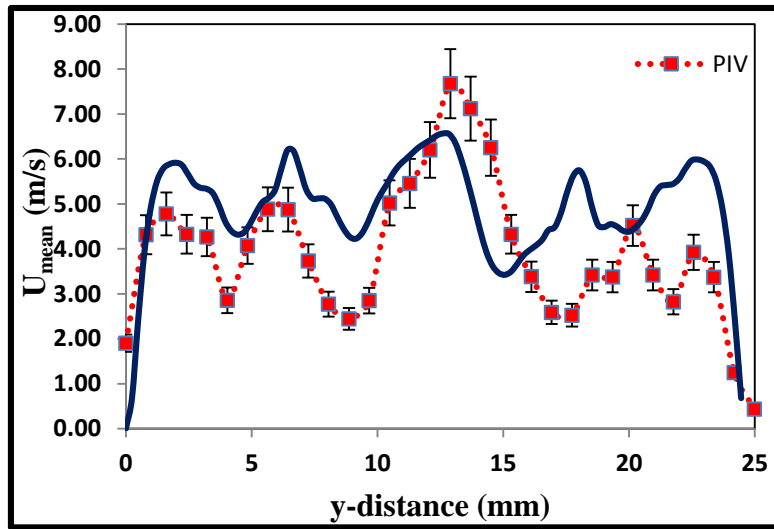


Figure 5.1: Average  $u$  velocity profile after grid comparison between CFD and PIV results [28]

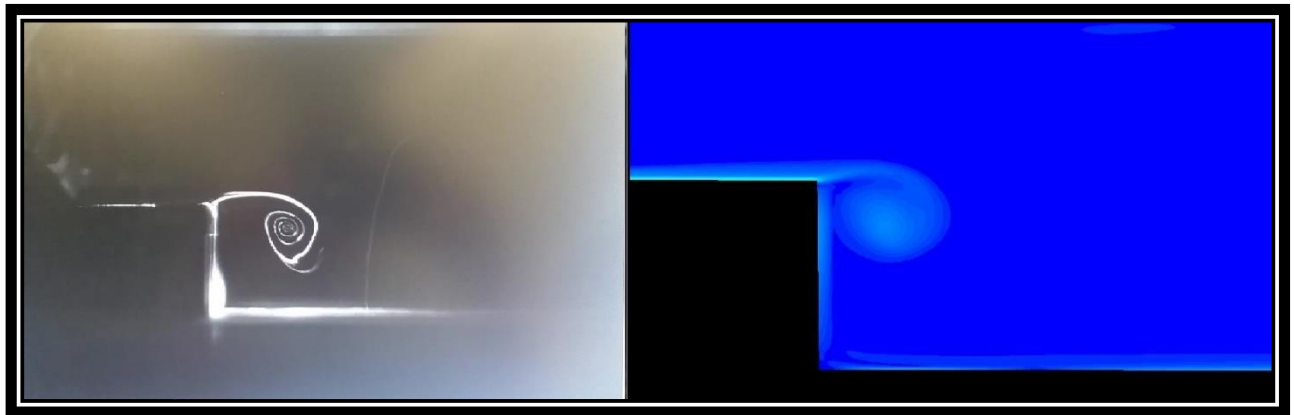


Figure 5.2: comparison of PIV images and CFD results for  $Re = 850$

## 5.1 Particle Image Velocimetry (PIV) Testing

The results of the experiments carried out for the present work are summarized in Table 5.1. Three sets of images were generated per blockage ratio and flow condition, equaling a total of 27 image sets for analysis. Of those image sets, further analysis narrowed down the post-processing to 9 image sets, with 375 images per analysis. The results of post-processing are presented in the next sections to show how the flow structures differ per grid and flow rate. The results from PIV imaging were taken at a line before the step and one after the step (Figure 5.1) to analyze the flow structure changes caused by the backward facing step. From the images, proper orthogonal decomposition (POD) analysis, kinetic energy measurement, and turbulent intensity measurements were obtained.

Table 5.1: Summarization of flow condition results

Blockage Ratio (%)	Flow Rate (scfm)	Re	Proportional Valve Voltage
67	25	4852	3.5
67	55	10675	4.2
67	115	22321	5.7
61	25	5307	3.5
61	55	11676	4.2
61	115	24413	5.7
54	25	5762	3.5
54	55	12676	4.2
54	115	26506	5.7

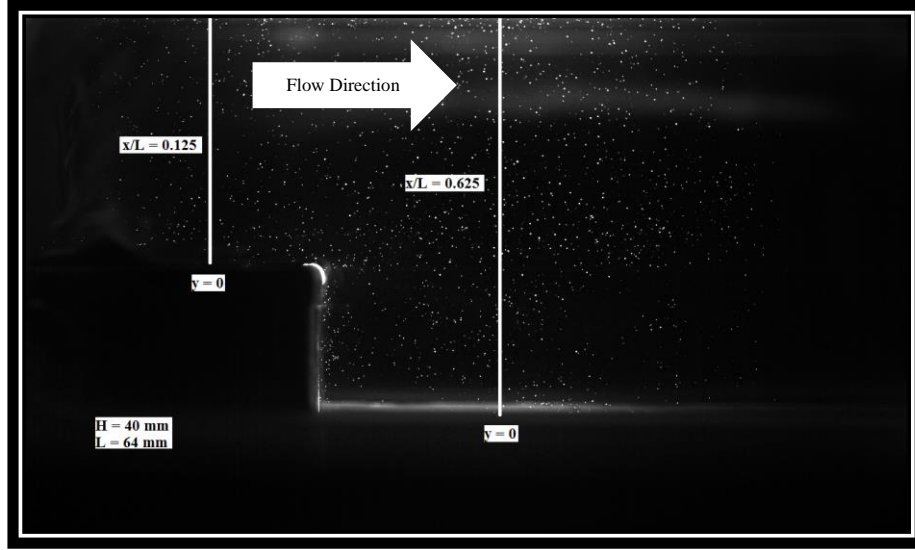


Figure 5.3: Area of interest for PIV analysis with lines indicating location of data extraction

### 5.1.1 PROPER ORTHOGONAL DECOMPOSITION RESULTS

Proper orthogonal decomposition (POD) is a post-processing technique offered in ‘DynamicStudios’ which allows PIV data to be decomposed into different energy modes. First a snapshot is taken from a range of images which gives a graphical representation of the energy decomposition in the flow. The mean velocity field is considered the zero'th mode of the POD. Subtracting the mean from all snapshots, the rest of the analysis operates on the fluctuating parts of the velocity components ( $u_{mn}$ ,  $v_{mn}$ ,  $w_{mn}$ ) where  $u$ ,  $v$  &  $w$  denote the fluctuating part of each velocity component [29]. The fluctuation components are then resolved into a multi-dimensional matrix and decomposed into the different energy modes in the flow. Figure 5.4 shows a sample POD snapshot, Appendix IV has a complete list of all POD snapshots. This snapshot is then projected onto the PIV images to isolate the flow structure according to the chosen energy modes. The POD projections for the three blockage ratios are presented in Figures 5.5 - 5.10.

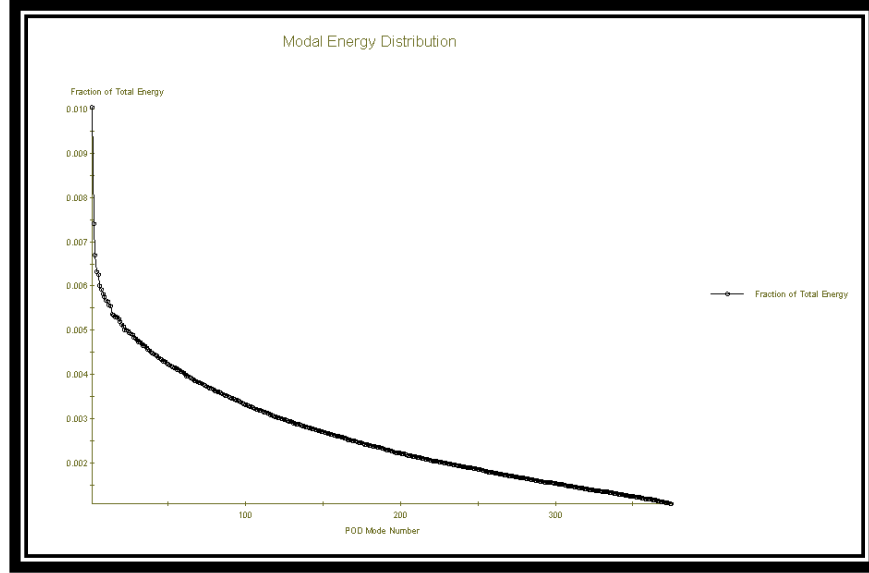


Figure 5.4: Sample POD snapshot for BR 67% and  $Re = 22321$

When carrying a POD analysis, the POD snapshot is crucial to the validation of results. The snapshot should exhibit an exponential decrease in energy as mode number increases. This indicates the concentration of energy in the first modes which are associated with the largest scales in the fluid. This analysis provides a quantification of the integral length scale,  $L_T$ , defined in Chapter 2. The lower energy modes are noise and therefore not of interest.

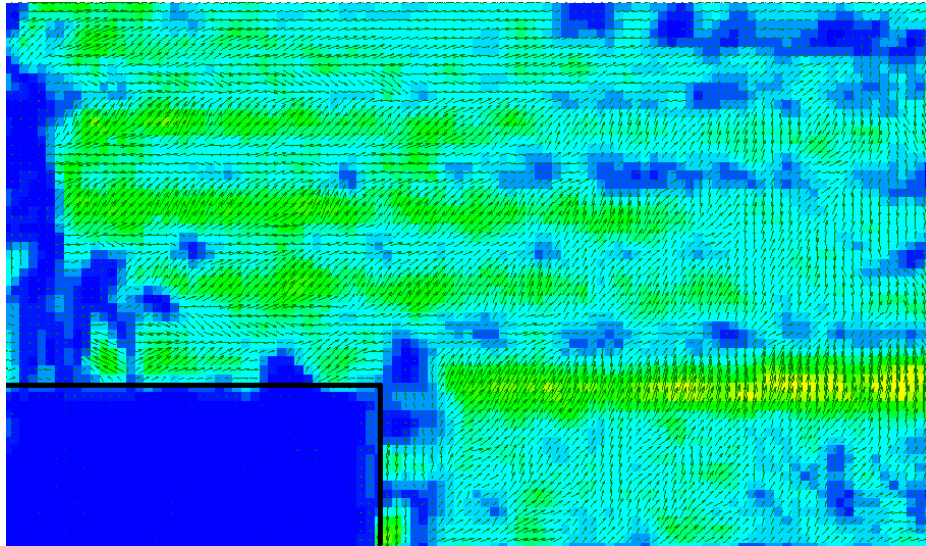


Figure 5.5: POD projection with 67% BR and  $Re = 22321$



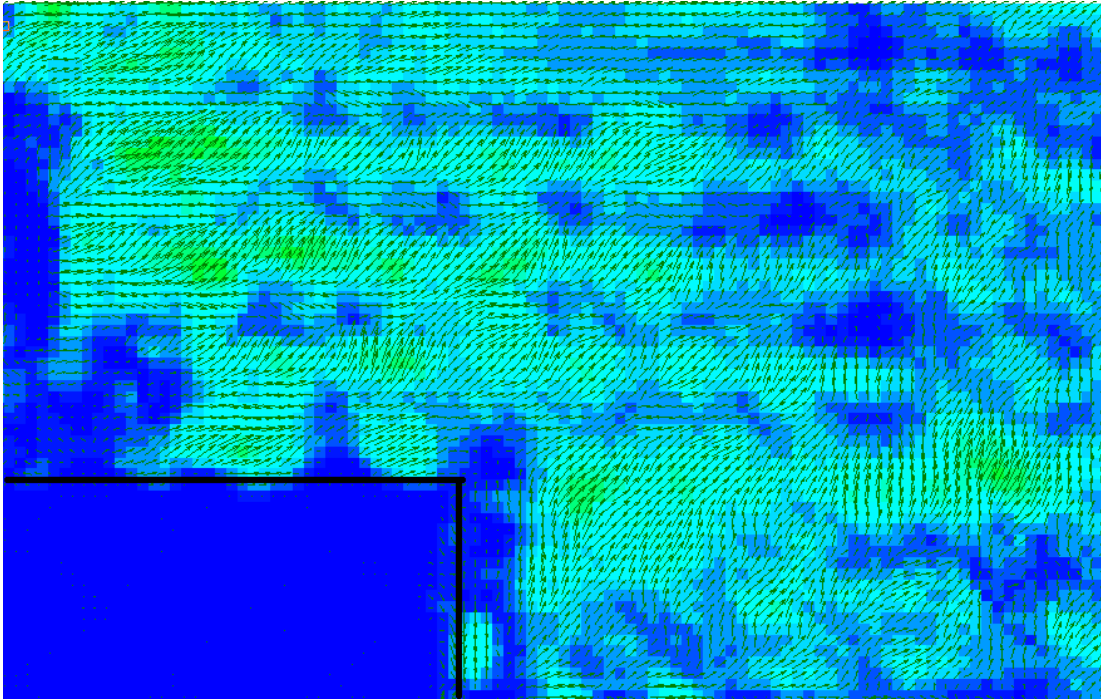


Figure 5.6: POD projection with 67% BR and  $Re = 10765$

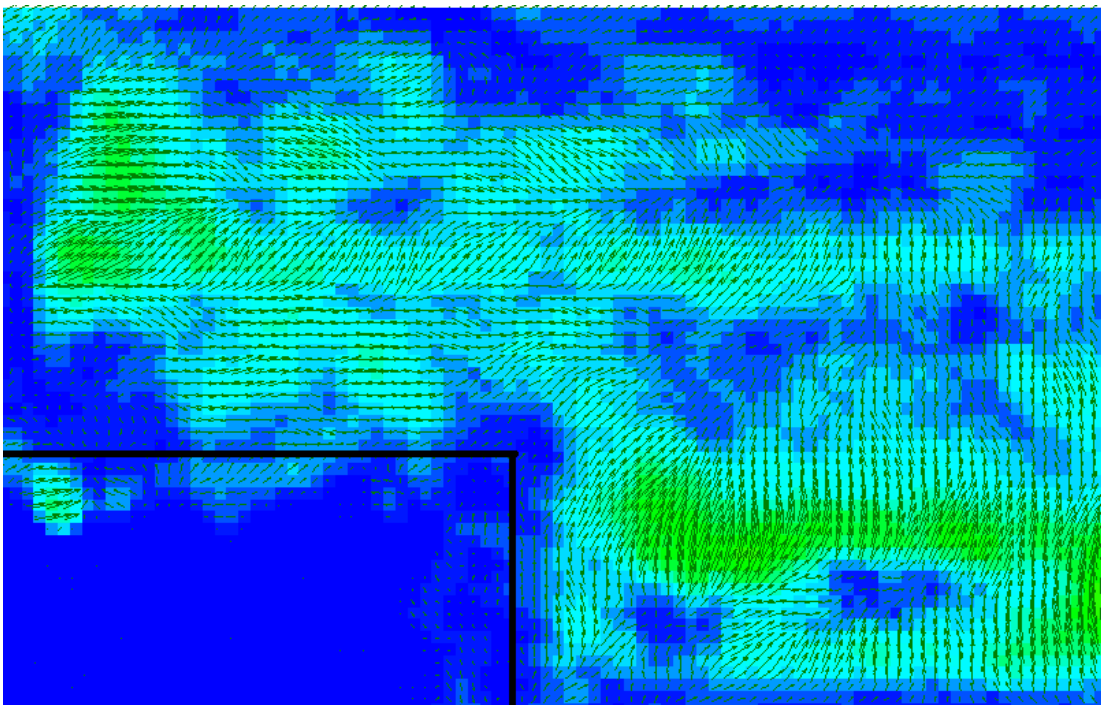


Figure 5.7: POD projection with 61% BR and  $Re = 24413$

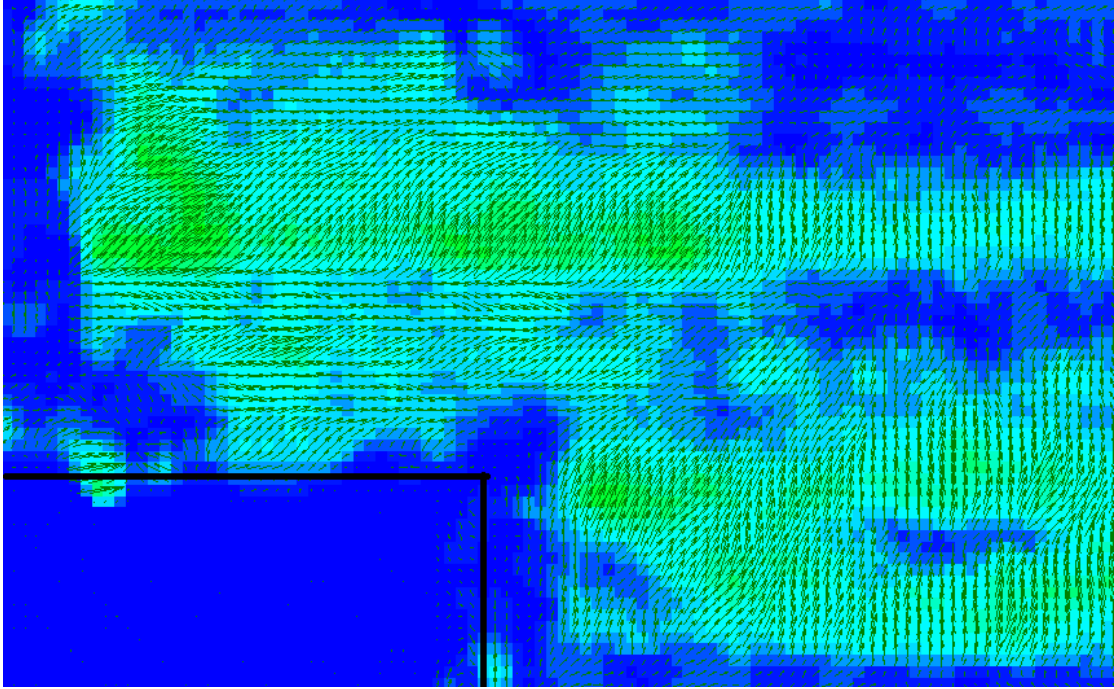


Figure 5.8: POD projection with 61% BR and  $Re = 11676$

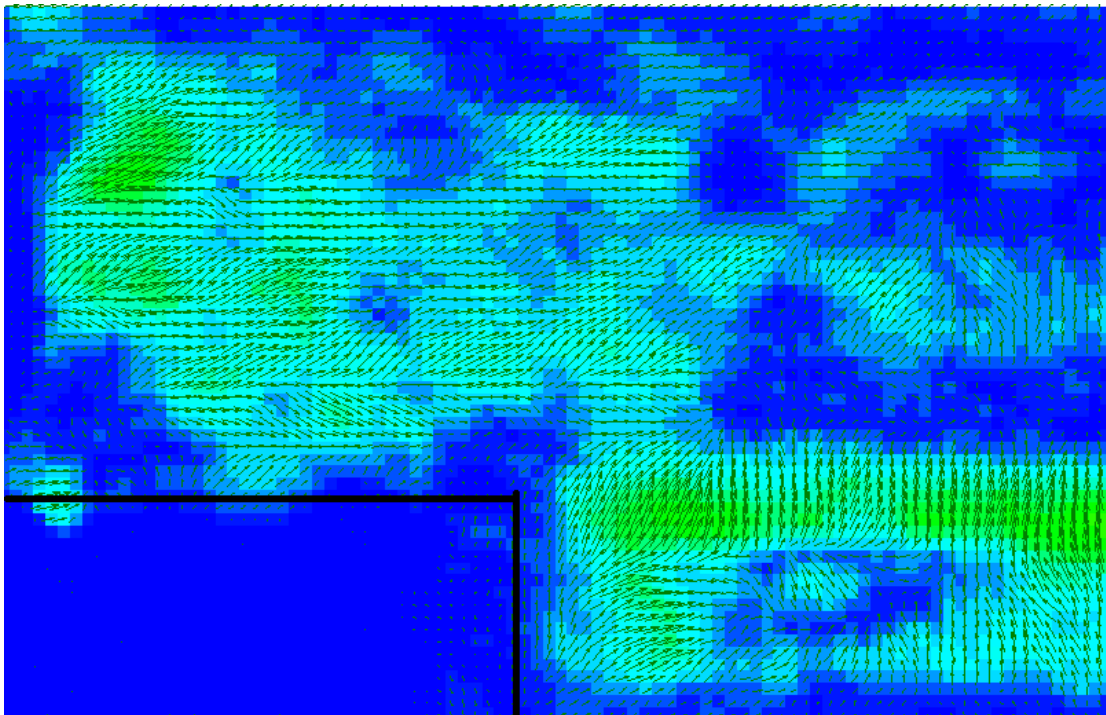


Figure 5.9: POD projection with 54% BR and  $Re = 26506$



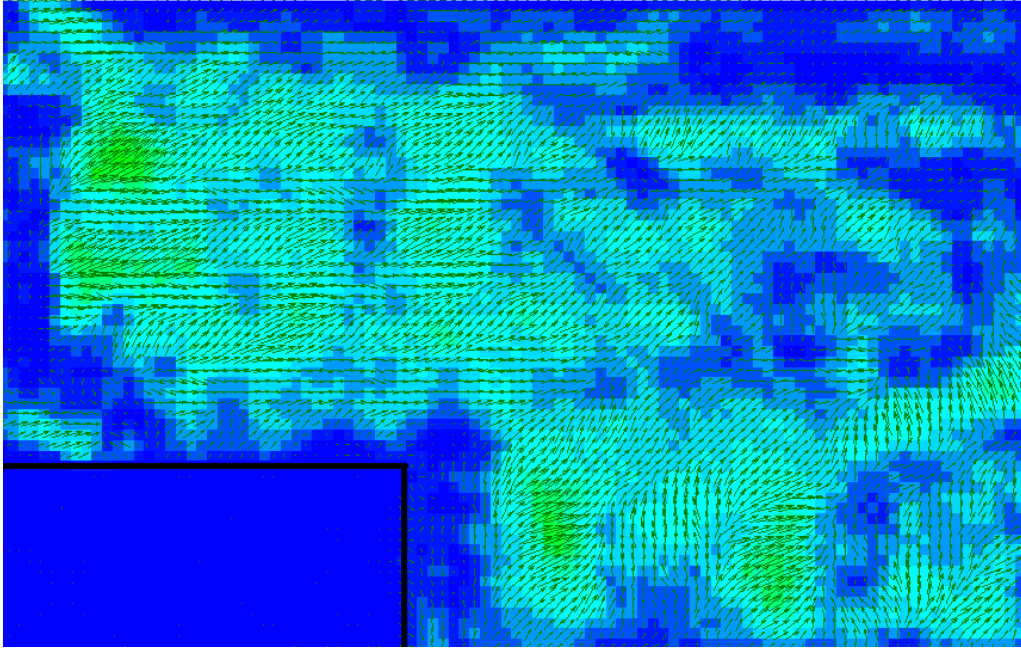


Figure 5.10: POD projection with 54% BR and  $Re = 12676$

The POD analysis shows a comparison between lower and higher Reynolds numbers, and shows the structural difference in the energy modes. The modes represent the structures which carry the highest amount of energy. The largest energy concentration regions follows a similar pattern for all cases. In the lower flow cases (Figures 5.6, 5.8 and 5.10) the flow carries the highest energy at the entrance of the combustor and at the region in the step. Clear recirculation is only seen in Figure 5.10 and 5.8 however, and in Figure 5.6 there is a shear layer which cause the flow to separate after the step. In figure 5.6 the appearance of jets caused by the perforated plate can be seen, and these jets break up once the flow passes the step. In the higher flow cases the flow structures are dominated by the entrance regions and shear layers similar to that shown in Figure 5.6. The appearance of jets is apparent on Figures 5.5, 5.7 and 5.9 though only Figure 5.5 shows clearly defined flow jets which carry past the light sheet area. Figure 5.7 also shows a clear jet in the center of the flow profile, though this jet breaks up before the end of the light sheet. Though Figure 5.9 exhibits favorable breakup, the shear layer in Figure 5.7 shows a reattachment point toward the end of the light sheet.

### 5.1.2 MEASUREMENT OF KINETIC ENERGY

The kinetic energy distribution is compared for the three grids at the lines before and after the step. Equation 2.6 is used to calculate the turbulent kinetic energy, and these values are then normalized when plotted. The results of kinetic energy with respect to y – position of a particle are shown in Figure 5.12 – Figure 5.15. The normalized kinetic energy will serve as a way to analyze how the energy is distributed before and after the step, as well as to show how this energy increases when flow rate is increased. Figure 5.11 shows a general visual representation of kinetic energy distribution in the flow field.

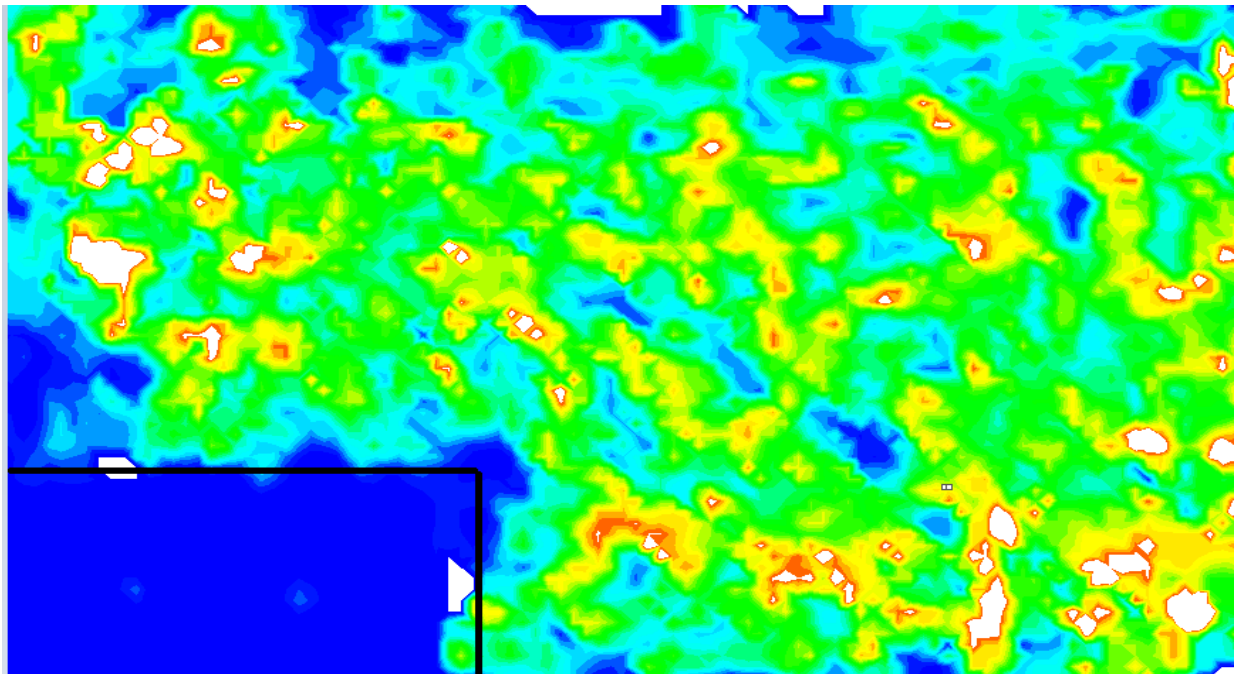


Figure 5.11: Kinetic energy distribution in the flow shown for 67% BR at  $Re = 22321$

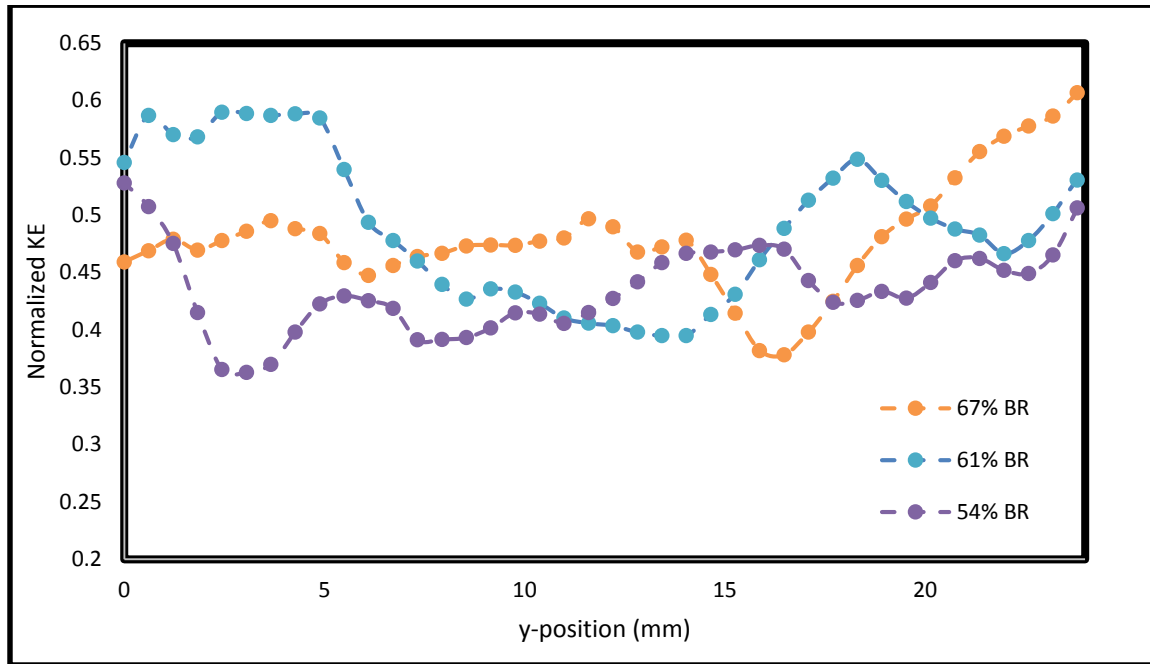


Figure 5.12: Normalized kinetic energy before the step for BR = 54%, 61% and 67% at Re = 12676, 11676 and 10675 respectively

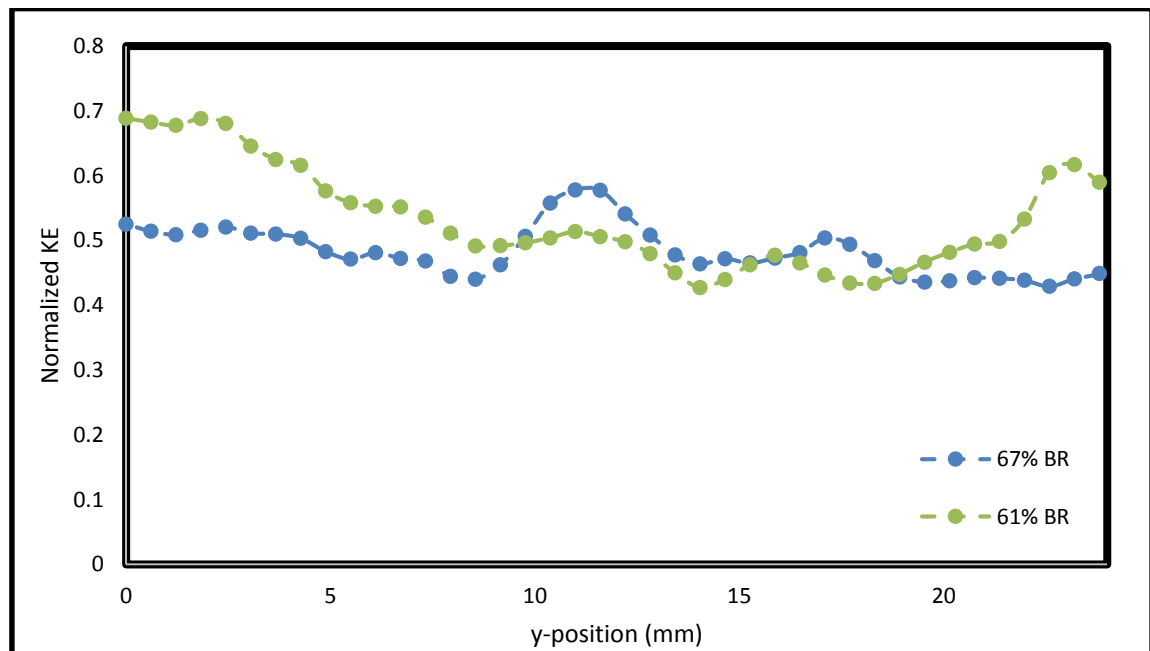


Figure 5.13: Normalized kinetic energy before step for 67% and 61% BR at 22321 and 24413 respectively

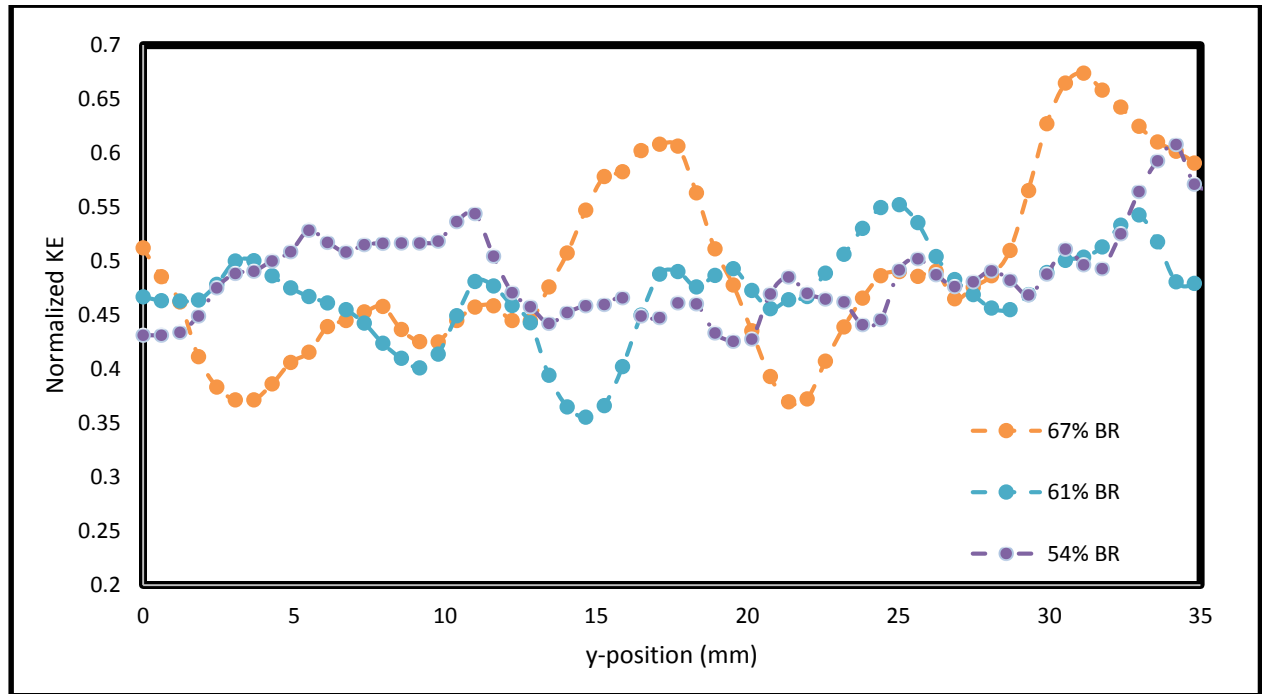


Figure 5.14: Normalized kinetic energy after the step for BR = 54%, 61% and 67% at Re = 12676, 11676 and 10675 respectively

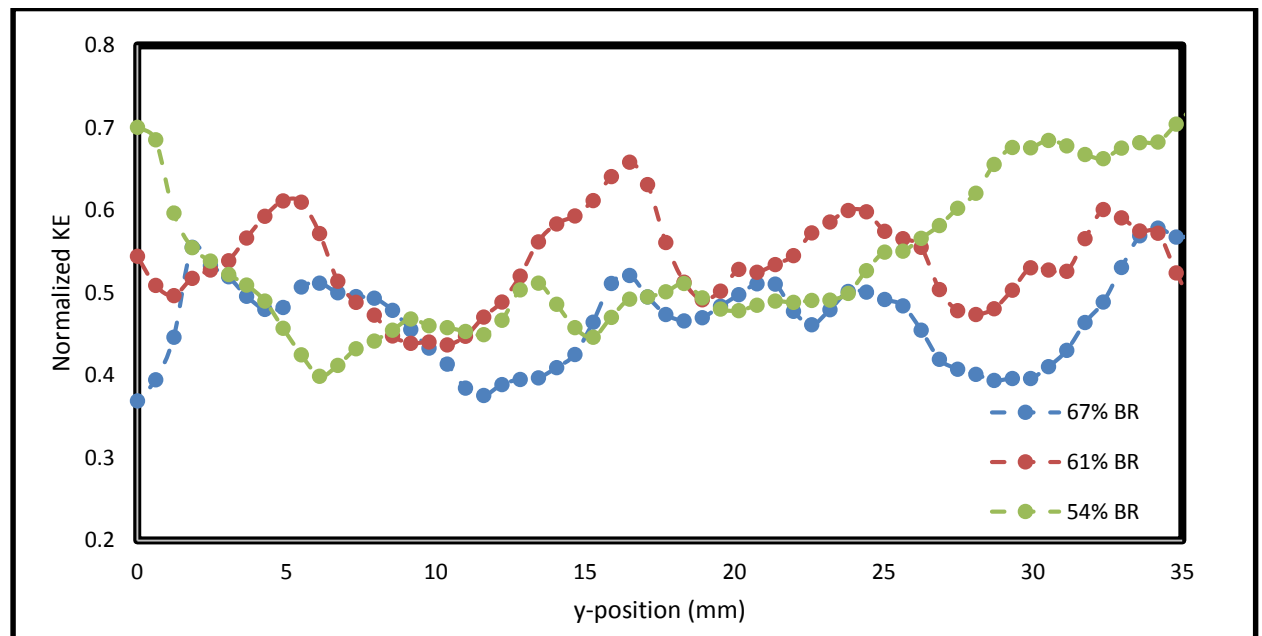


Figure 5.15: Normalized kinetic energy after the step for BR = 54%, 61% and 67% at Re = 26506, 24413 and 22321 respectively

At the lower flow rate, BR = 67% has the most TKE compared to the other two grid geometries, but at the higher flow rates the TKE favors BR = 61% both before and after the step. Figure 5.14 shows the three grid TKE values follow a similar trend caused by the grid induced turbulence. Much like in the POD analysis, the BR = 67% shows less breakup in the flow as seen by the drop in TKE shown in Figure 5.15. Again at higher flow rates the BR which shows promising values is 61%.

### 5.1.3 MEASUREMENT OF TURBULENT INTENSITY

The turbulent intensity is an important parameter in determining turbulence in the flow, and more importantly the velocity fluctuations described in Section 2.4. General values of turbulent intensity range from 5 – 20%. Turbulent intensity is calculated before and after the step and compared for the different grid geometries and flow rates. Equation 2.5 is used to calculate the value of turbulent intensity. The results for turbulent intensity are presented in Figure 5.16 – Figure 5.19.

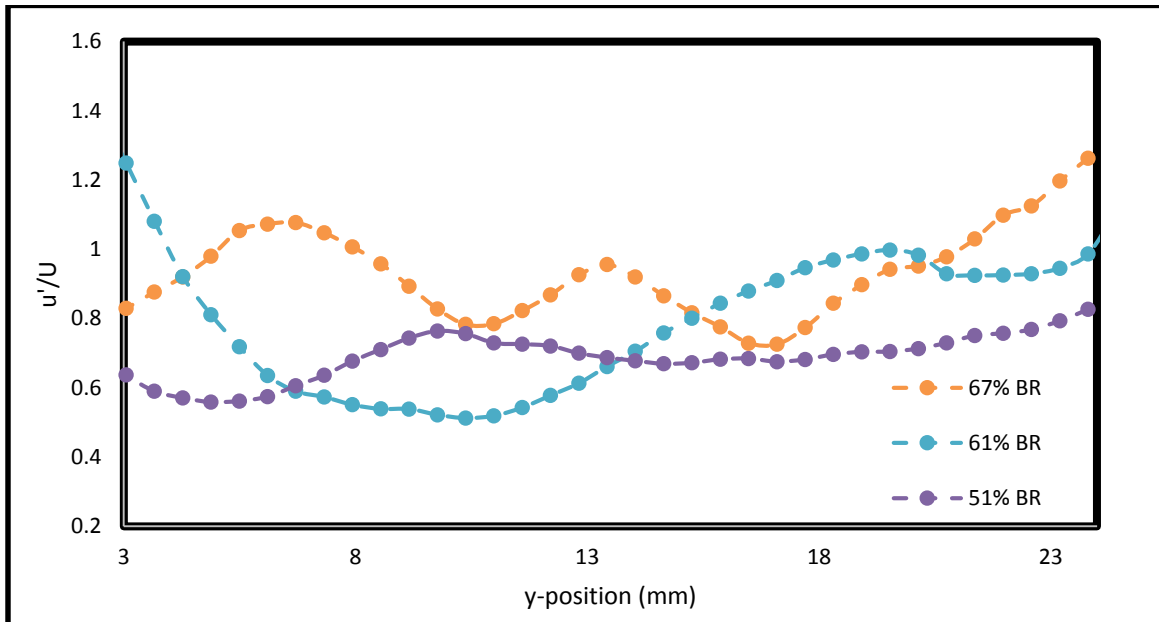


Figure 5.16: Turbulent intensity before step with BR = 54%, 61% and 67% and Re = 12676, 11676 and 10675 respectively

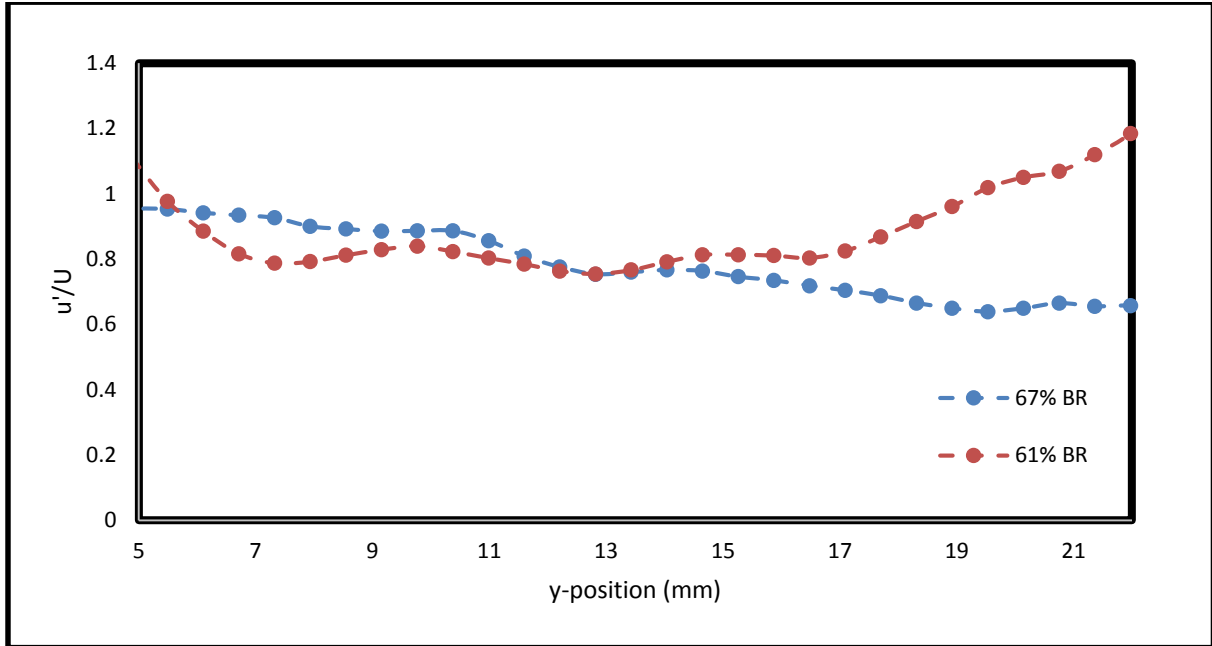


Figure 5.17: Turbulent intensity before step for BR = 67% and 61% with Re = 24413 and 22321 respectively

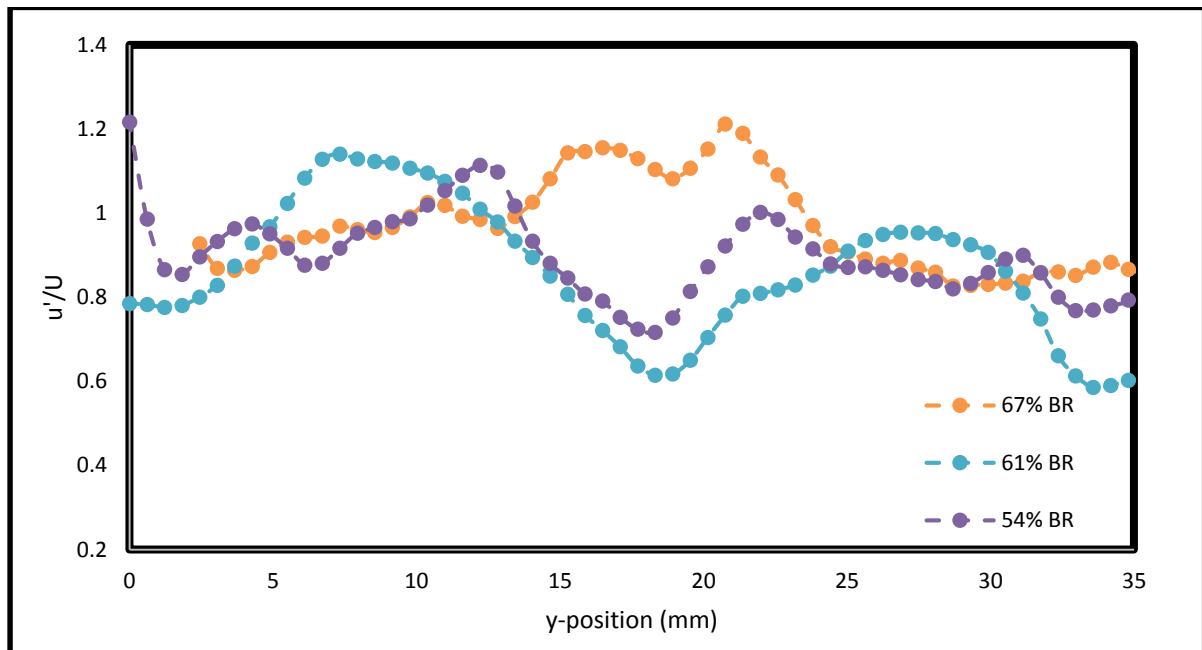


Figure 5.18: Turbulent intensity after the step with BR = 54%, 61% and 67% and Re = 12676, 11676 and 10675 respectively

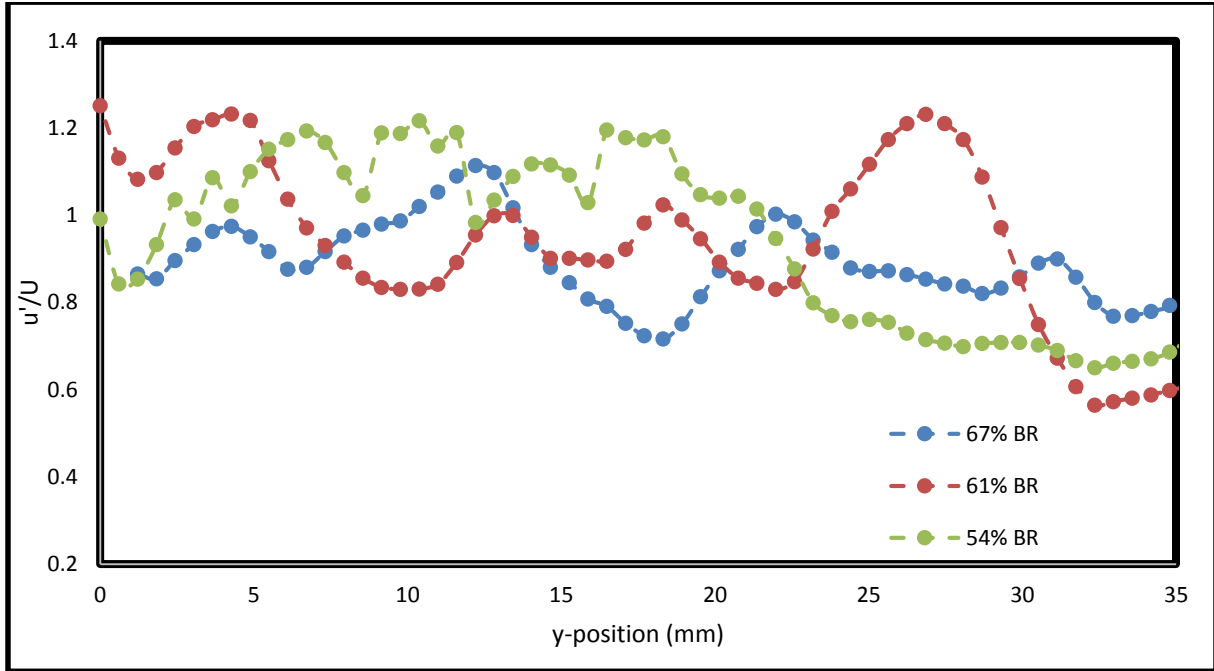


Figure 5.19: Turbulent intensity after the step with BR = 54%, 61% and 67% and Re = 26506, 24413 and 22321 respectively

Again BR = 67% exhibits greater turbulent intensity at lower flow rate values, but drops in the case of maximum flow. Figure 5.16 and Figure 5.18 show the BR = 67% turbulence intensity is greater than the other grids which validates this assumption. Figure 5.19 shows how the turbulent intensity in BR = 67% drops below the other grids and BR = 61% is the dominant turbulence generator; this assumption is also validated in Figure 5.17. It should be noted that in Figure 5.17 the turbulent intensity follows a parabolic profile which has a peak at the bottom and top surfaces of the combustor. This behavior can be attributed to the formation of jets seen in the POD analysis for both BR = 67% and 61%. This parabolic profile is not apparent in Figures 5.16 and 5.18, correlating to the formation of the jets at higher flow rates shown in the POD analysis. Figure 5.19 illustrates a more predictable trend for turbulent intensity in the grids meaning the jets begin breaking up, causing fluctuations in the flow field.

#### 5.1.4 COMPARISON OF GRID THICKNESS

From the previous analyses, it was determined that the formation of jets affects the behaviors of the flow and causes the grid to act as an orifice rather than a turbulent generator. In order to address this issue, the  $BR = 67\%$  grid was duplicated and its thickness was halved. This  $BR$  was chosen due to being the most affected by the jet formation in the previous sections. Figure 5.20 shows a POD projection for the thinner grid, Figure 5.21 shows a comparison of TKE, and Figure 5.22 shows a comparison of turbulent intensity. The purpose of changing the grid thickness was to determine whether significant improvements are made to the flow structure in order to warrant a more detailed analysis of the grid geometry.

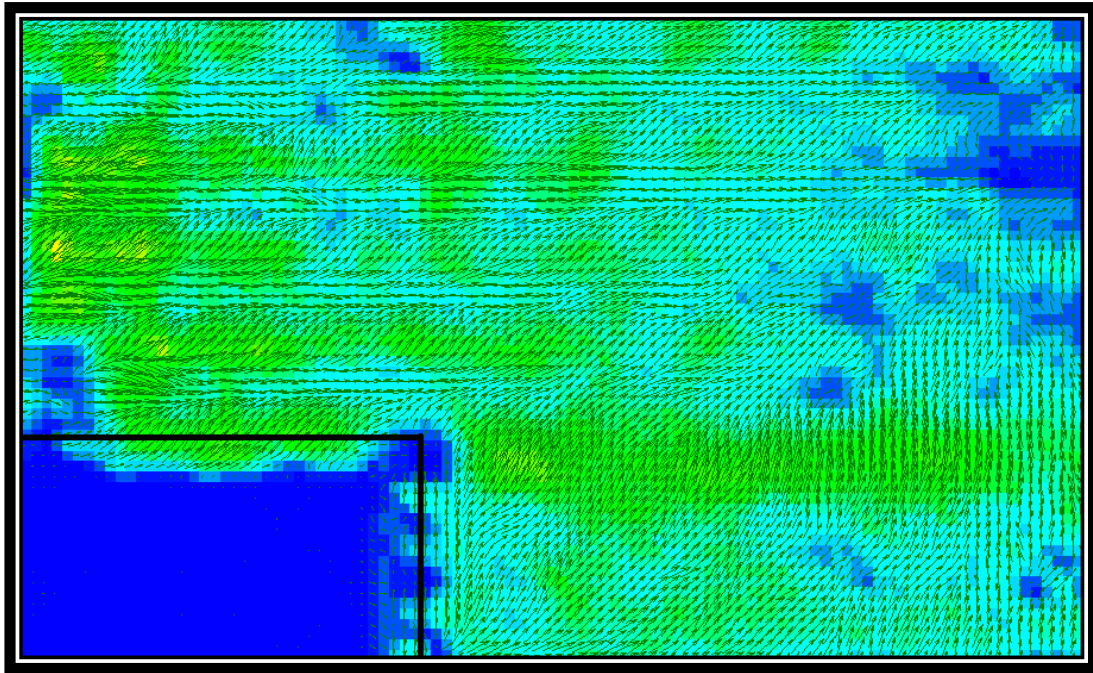


Figure 5.20: POD projection of thin grid  $BR = 67\%$  and  $Re = 22321$

Comparing Figure 5.20 to Figure 5.5 shows a dramatic change in flow structure. The jets begin breaking up much sooner in the thin grid, and there is some recirculation apparent under the shear layer after the step. Previously the length was determined by the size of the jets, which were assumed to be the size of the perforations in the grid.



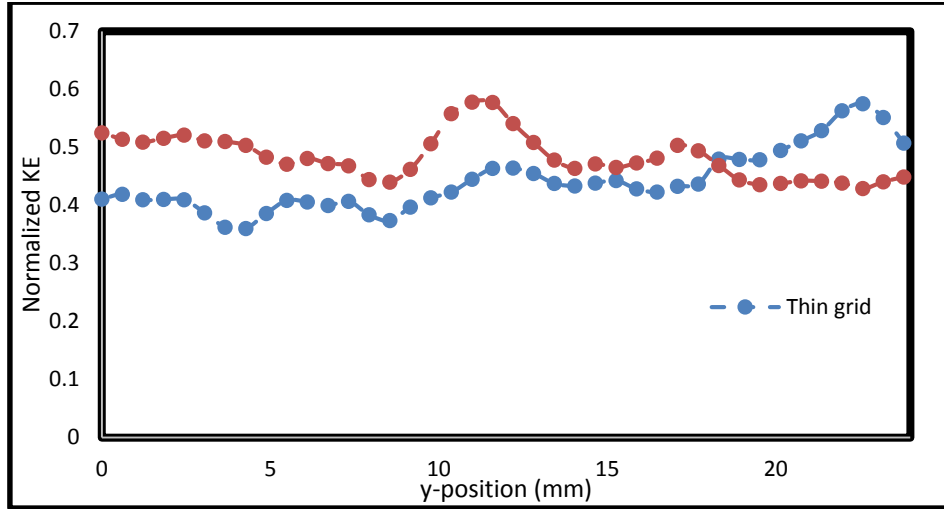


Figure 5.21: Normalized kinetic energy for regular and thin grid at BR = 67% and Re = 22321

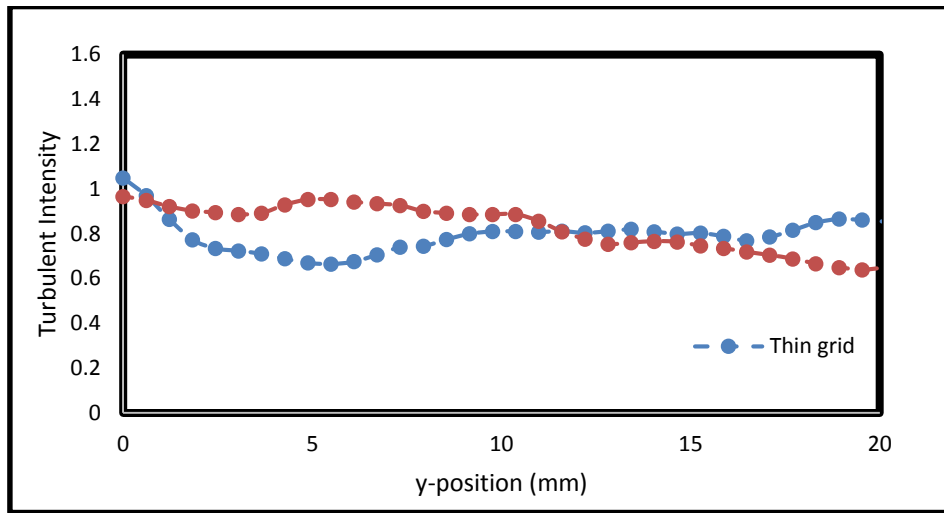


Figure 5.22: Turbulent intensity comparison between regular and thin 67% BR at Re = 22321

Figure 5.21 and Figure 5.22 show the values of TKE and turbulent intensity do not vary dramatically with the change in grid thickness. Figure 5.21 shows a slight increase in TKE for the thinner grid which can be attributed to the earlier breakup of the jets. Figure 5.22 however shows the turbulent intensity remains unchanged for the two grids. The results of changing the grid thickness suggest a further investigation of grid geometry should be conducted to find an optimal grid geometry.

## Chapter 6: Conclusion and Future Work

### 6.1 Summary

Flow mapping of a high turbulent intensity combustor has been completed. An analysis of high Reynolds number fluid flow over a backward facing step has been performed using PIV imaging. Results of the analysis indicate the grid geometry has a great effect on flow structure as evidenced by the results; the conclusion being that a thinner grid with blockage ratio = 61% provides better flow breakup. These results confirm the presence of high turbulence in the system, and the varying length scales associated with different geometries. The three main parameters were resolved for different turbulent flow rates, including compressible flow. These three main parameters serve to further the understanding of flow interactions and how these affect the turbulent parameters required to achieve a thickened flame.

- POD analysis: provides a method of isolating the energy modes in a flow to determine structural parameters ( $L_T$ )
- Kinetic Energy: provides additional flow mapping and denotes the profiles in which the largest energy is carried by the flow
- Turbulent Intensity: Determines the ratio of turbulence affecting the flow field in order to quantify velocity fluctuations in a flow ( $u'$ )

These parameters, along with combustion parameters, will determine the flame regime studies for the high turbulent intensity system.

## 6.2 Future Work

Further grid studies can be performed in order to find an optimization point for grid blockage ration and thickness. Furthermore the combustion system is ready to begin testing and analyzing flame behavior. The further considerations of the project can be described as follows:

- To further the development of a backward facing step stabilized flame system by conducting initial flame studies using PLIF.
- To study flow and flame characteristics using simultaneous Time Resolved Particle Image Velocimetry (TR-PIV) and OH/CH Planer Laser Induced Fluorescence (PLIF) imaging.
- To define the effects of bulk velocity parameters, turbulence parameters and recirculation zone characteristics on flame location, shape, fluctuation, reaction zone and local displacement speed.

The findings presented in this work will be used with the future flame studies in order to determine and characterize a thickened flame. The experimental findings of a flame in the thin reaction zone regime will provide useful data to develop numerical and computational models which can be applied to the design of high turbulent combustion systems.

## References

- [1] Durst, F., and Pereira, J. C. F., 1988, "Time-dependent laminar backward facing step flow in a two-dimensional duct", ASME J. Fluids Eng., 110, pp. 289–296.
- [2] So RMC, Yuan SP. "Near-wall Two-equation and Reynolds-stress Modeling of Backstep Flow". Int. J. Engng Sci. Vol. 36, No. 3, pp. 283-298, 1998.
- [3] Biswas G, Breuer M, Durst F. "Backward-Facing Step Flows for Various Expansion Ratios at Low and Moderate Reynolds Numbers". Journal of Fluids Engineering MAY 2004, Vol. 126.
- [4] Armaly BF, Durst F, Pereira JCF, Schönung B. "Experimental and theoretical investigation of backward-facing step flow". J. Fluid Mech. (1983), vol. 127, p p. 473496.
- [5] Acosta-Zamora A., Choudhuri A., Hossain M. A., Quiroz M. (2014). "Design of a High Turbulence Intensity Combustion System". Paper presented at the 50th AIAA/ASME/SAE/ASEE Joint Propulsion Conference, Cleveland, Ohio. July 28 – 30.
- [6] Reynolds, O. "An experimental investigation of the circumstances which determine whether the motion of water shall be direct or sinuous, and the law of resistance in parallel channels." Philos. R. Soc. London Ser. A 186, 935-982.
- [7] O'Connor, John J., Robertson, Edmund F., "Osborne Reynolds", MacTutor History of Mathematics archive, University of St Andrews.
- [8] Cengel Yunus A., Cimbala John M., "Fluid Mechanics: Fundamentals and Applications, McGraw-Hill", 2006
- [9] Pope S.B. "Turbulent Flow", Cambridge university press, 2000.

- [10] “Basics of turbulent flow”, [www.mit.edu](http://www.mit.edu), accessed 2015
- [11] Richardson, L. F. (1992). “Weather Prediction by Numerical Process”. Cambridge: Cambridge University Press.
- [12] Kolmogorov, A.N. (1941a), “Dissipation of energy in locally isotropic turbulence.” Dokl. Akad. Nauk SSSR 32, 19-21
- [13] Davidson P.A., 'Turbulence, An Introduction for scientists and engineers' Oxford University Press 2004
- [14] Hoinghaus K.K., Jeffries J.B.. “Applied Combustion Diagnostics”, Taylor and Francis, 2002
- [15] Adrian, R.J. (1991). “Particle-Imaging Techniques for Experimental Fluid Mechanics”. Annual Review of Fluid Mechanics 23: 261-304
- [16] Raffel M., Willert C. E., Kompenhans J. “Particle Image Velocimetry: A Practical Guide”. Springer, Berlin; New York. 1998
- [17] F. Grisch, M. Orain, “Role of Planar Laser-Induced Fluorescence in Combustion Research”, Journal Aerospace Lab, 2009
- [18] Barlow R. S., “Laser diagnostics and their interplay with computations to understand turbulent combustion”. Proceedings of the Combustion Institute 31. 49-57. 2007

- [19] B. Li, Z. W. Sun, J. Zetterberg, Z Li, M. Aldén, “Visualization of Radicals”, Lund University, 2008
- [20] Borghi, R., “On the structure and Morphology of Turbulent Premixed Flames”. Recent Advances in Aeronautical Science. Plenum Press, New York. 1985
- [21] Peters, N., “The turbulent burning velocity for small-scale and large-scale turbulence”. J. Fluid Mech., 1999. 384: p. 107-132.
- [22] Zimont, V., Theory of turbulent combustion of homogenous fuel mixture at high Reynolds numbers. Fizika Goreniya i Vzryva, 1979. 15: p. 23-32.
- [23] Choudhuri A. R., “Investigation on the Flame Extinction Limit of Fuel Blends”, Combustion and Propulsion Research Laboratory, Mechanical and Industrial Engineering Department, The University of Texas at El Paso
- [24] James J. E. A., “Gas Dynamics”, Pearson Prentice Hall, 2006
- [25] Dynalene Inc., HC series [data sheet](#), accessed 2014
- [26] Cengel Y. A., “Heat and Mass Transfer”, 3<sup>rd</sup> edition, McGraw Hill, 2006
- [27] “Thermal Expansion”, [www.rice.edu](http://www.rice.edu), accessed 2015
- [28] Hossain M. A., “Design of a High Intensity Turbulent Combustion System”, University of Texas at El Paso, 2015
- [29] Dantec Dynamics, “DynamicStudios Manual”, 2013

## Appendix I

Specification of pressure transducers and thermocouples.

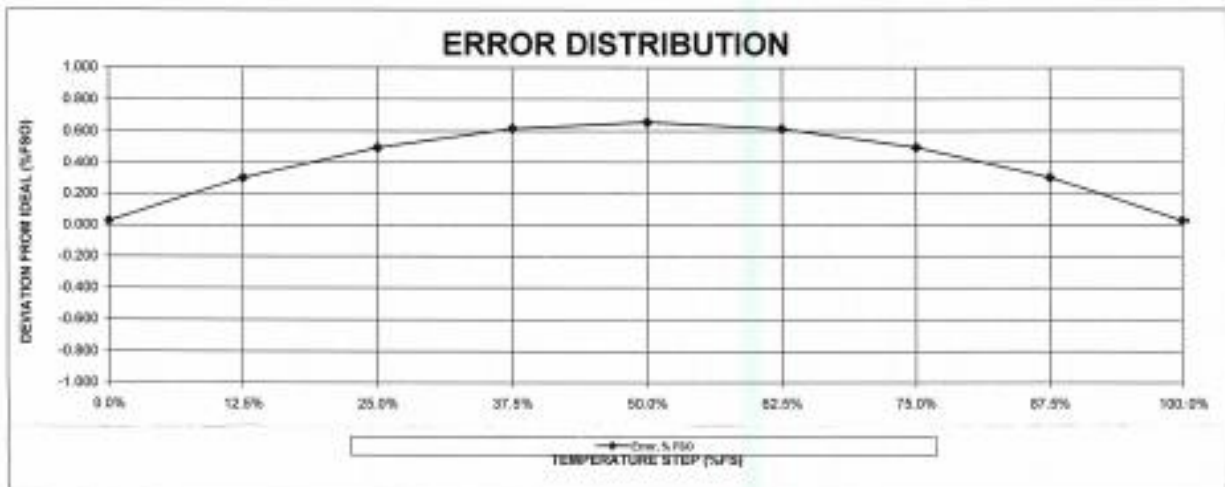
<b>LORD STI</b> STELLAR TECHNOLOGY	<i>TC-02</i>	237 Commerce Drive Amherst, New York 14228 USA Tel: 716.250.1900 • Fax: 716.250.1909
------------------------------------	--------------	--

### TEMPERATURE CALIBRATION RECORD

<b>CUSTOMER</b> University of Texas @ El Paso	<b>SERIES/PART NUMBER</b> PT1700-150G-171	<b>SERIAL NUMBER</b> 1401446	<b>SALES ORDER</b> 14-0026
<b>CUSTOMER PO</b> 2014047243	<b>CUSTOMER PART NUMBER</b> N/A	<b>MAX/CAL VOLTAGE</b> 18/12 Vdc	
<b>TEMP. RANGE (°F)</b> 0 TO 300	<b>OUTPUT RANGE</b> 0-5 V	<b>CONDITION</b> NEW	

ALL DATA IN °F

STEP	TEMP. (°F)	Output, V	Ideal, V	Error, V	Error, % FSO
0.0%	0.000	0.001	0.000	0.001	0.026
12.5%	37.500	0.640	0.625	0.015	0.301
25.0%	75.000	1.275	1.250	0.025	0.498
37.5%	112.500	1.906	1.875	0.031	0.615
50.0%	150.000	2.533	2.500	0.033	0.654
62.5%	187.500	3.156	3.125	0.031	0.615
75.0%	225.000	3.775	3.750	0.025	0.497
87.5%	262.500	4.390	4.375	0.015	0.301
100.0%	300.000	5.001	5.000	0.001	0.026



SUMMARY			CONNECTIONS		MISC
VALIDATION POINT	149.0°F	2.516	PIN	DESCRIPTION	CONNECTOR
STATIC ACCURACY (% FSO)		0.654	A	EXC+	202031
			D	EXC-	CAL. REC. NO.
			B	PSIG+	41912.42388
			C	PSIG-	QA STAMP
			E	TSIG+	
			F	TSIG-	
					9/30/2014

DCN 808

201905F

TC-4

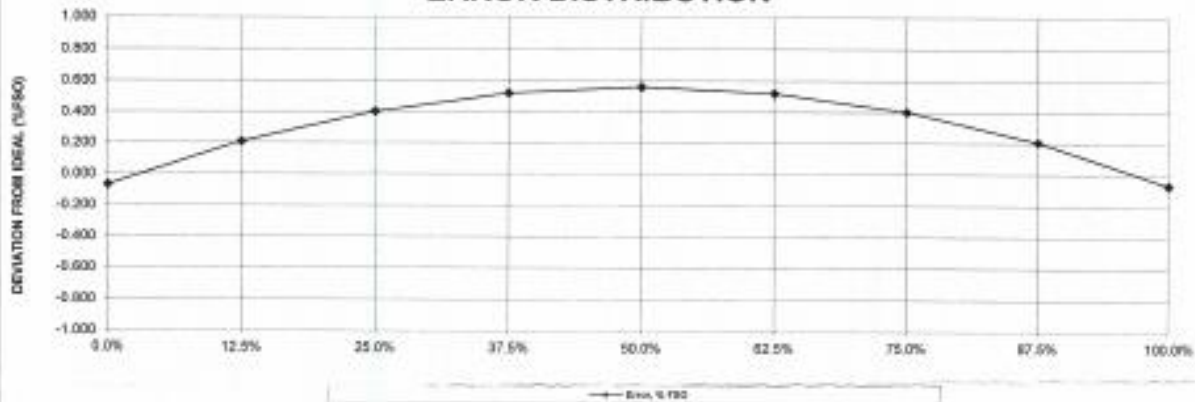
### TEMPERATURE CALIBRATION RECORD

<b>CUSTOMER</b>	<b>SERIES/PART NUMBER</b>	<b>SERIAL NUMBER</b>	<b>SALES ORDER</b>
University of Texas @ El Paso	PT1700-150G-171	1401447	14-0026
<b>CUSTOMER PO</b>	<b>CUSTOMER PART NUMBER</b>	<b>MAX/CAL VOLTAGE</b>	
2014047243	N/A	18/12 Vdc	
<b>TEMP. RANGE (°F)</b>	<b>OUTPUT RANGE</b>	<b>CONDITION</b>	
0 TO 300	0-5 V	NEW	

ALL DATA IN °F

STEP	TEMP.(°F)	Output, V	Ideal, V	Error, V	Error, % FSO
0.0%	0.000	-0.003	0.000	-0.003	-0.068
12.5%	37.500	0.635	0.625	0.010	0.207
25.0%	75.000	1.270	1.250	0.020	0.403
37.5%	112.500	1.901	1.875	0.026	0.521
50.0%	150.000	2.528	2.500	0.028	0.560
62.5%	187.500	3.151	3.125	0.026	0.521
75.0%	225.000	3.770	3.750	0.020	0.403
87.5%	262.500	4.385	4.375	0.010	0.207
100.0%	300.000	4.997	5.000	-0.003	-0.068

### ERROR DISTRIBUTION



SUMMARY			CONNECTIONS		MISC
VALIDATION POINT	150.0°F	2.528	PIN	DESCRIPTION	CONNECTOR
STATIC ACCURACY (% FSO)		0.560	A	EXC+	202031
			D	EXC-	CAL. REC. NO.
			B	PSIG+	41912.56689
			C	PSIG-	QA STAMP
			E	TSIG+	
			F	TSIG-	

DCM 002

2014 002



**CALIBRATION RECORD**

CUSTOMER	SERIES/PART NUMBER	SERIAL NUMBER	SALES ORDER
University of Texas @ El Paso	PT1700-150G-171	1401446	14-0026
CUSTOMER PO	CUSTOMER PART NUMBER	PRESSURE RANGE	
2014047243	N/A	0-150 PSIG	
COMP. TEMP. RANGE (°F)	GAGE RESISTANCE	PROOF / BURST PRESSURE	
0 TO 250	5000	225/300	PSI
OPER. TEMP. RANGE (°F)	MAX/CAL VOLTAGE	CONDITION	
-65 TO 250	18/12 VOLTS	NEW	

ALL DATA IN V

TEST TEMPERATURE: AMBIENT

STEP	INCREASING			DECREASING			HYSTERESIS
	OUTPUT	BEST	DIFFERENCE	OUTPUT	BEST	DIFFERENCE	
0%	0.004	0.007	-0.003	0.008	0.007	0.001	0.004
20%	1.001	1.003	-0.002	1.004	1.003	0.001	0.003
40%	1.998	1.999	-0.001	2.001	1.999	0.002	0.003
60%	2.994	2.994	0.000	2.997	2.994	0.003	0.003
80%	3.990	3.990	0.000	3.991	3.990	0.001	0.001
100%	4.985	4.986	-0.001	4.985	4.986	-0.001	0.000
FSO	4.981					SHUNT	N/A

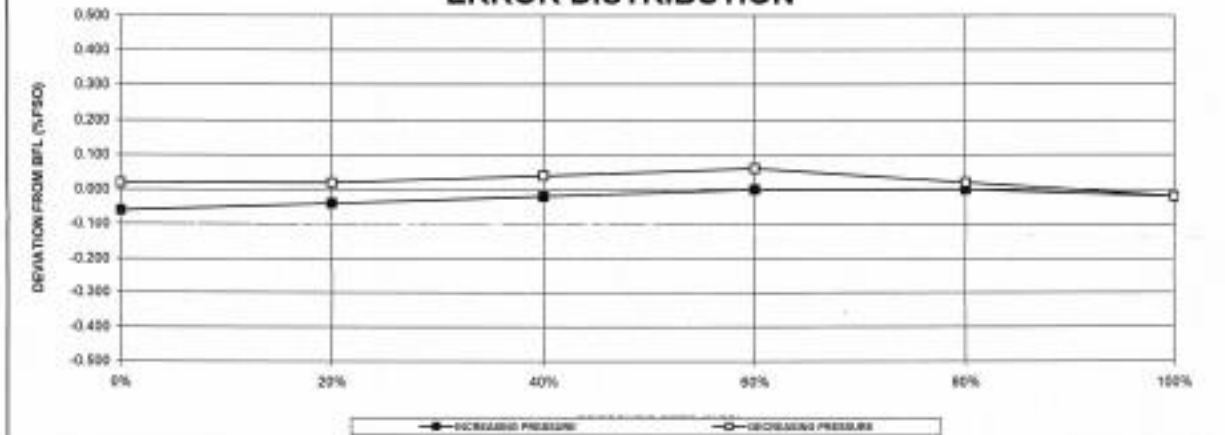
LOW TEMPERATURE: 0°F

HIGH TEMPERATURE: 250°F

REPEATABILITY @ AMBIENT

STEP	NORMALIZED	STEP	NORMALIZED
0%	0.014	0%	0.002
100%	4.993	100%	4.999
FSO	4.979	FSO	4.997

STEP	OUTPUT 1	OUTPUT 2
0%	-0.003	0.008
100%	4.979	4.982
FSO	4.982	4.982

**ERROR DISTRIBUTION**


SUMMARY		CONNECTIONS		MISC
ZERO BALANCE	0.004	PIN	DESCRIPTION	CONNECTOR
FULL SCALE OUTPUT	4.981	A	EXC+	202031
STATIC ACCURACY (%FSO)	0.060	D	EXC-	CAL REC. NO.
THERMAL ZERO SHIFT (%FSO / AMB TO HOT PER °F)	0.000	B	PSIG+	41912.42185
THERMAL ZERO SHIFT (%FSO / AMB TO COLD PER °F)	0.002	C	PSIG-	QA STAMP
THERMAL FSO SHIFT (%FSO / AMB TO HOT PER °F)	0.001	E	TSIG+	STI
THERMAL FSO SHIFT (%FSO / AMB TO COLD PER °F)	0.000	F	TSIG-	48
				QA
				9/30/2014

03/1/02/0

2/1/2/0/0

### CALIBRATION RECORD

<b>CUSTOMER</b>		<b>SERIES/PART NUMBER</b>	<b>SERIAL NUMBER</b>	<b>SALES ORDER</b>
University of Texas @ El Paso		PT1700-150G-171	1401447	14-0026
<b>CUSTOMER PO</b>		<b>CUSTOMER PART NUMBER</b>	<b>PRESSURE RANGE</b>	
2014047243		N/A	0-150 PSIG	
<b>COMP. TEMP. RANGE (°F)</b>		<b>GAGE RESISTANCE</b>	<b>PROOF / BURST PRESSURE</b>	
0 TO 250		5000	225/300	PSI
<b>OPER. TEMP. RANGE (°F)</b>		<b>MAXICAL VOLTAGE</b>	<b>CONDITION</b>	
-65 TO 250		18/12 VOLTS	NEW	

ALL DATA IN V

TEST TEMPERATURE: AMBIENT

STEP	INCREASING			DECREASING			HYSTERESIS
	OUTPUT	BEST	DIFFERENCE	OUTPUT	BEST	DIFFERENCE	
0%	-0.008	-0.006	-0.002	-0.006	-0.006	0.000	0.002
20%	0.989	0.990	-0.001	0.992	0.990	0.002	0.003
40%	1.987	1.987	0.000	1.989	1.987	0.002	0.002
60%	2.984	2.984	0.000	2.985	2.984	0.001	0.001
80%	3.980	3.980	0.000	3.981	3.980	0.001	0.001
100%	4.976	4.977	-0.001	4.976	4.977	-0.001	0.000
FSO	4.984					SHUNT	N/A

LOW TEMPERATURE: 0°F

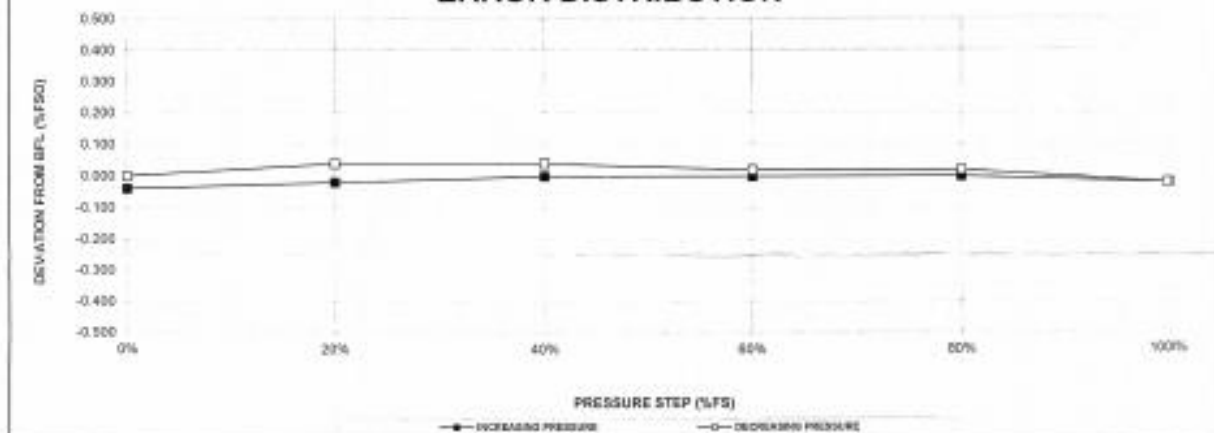
HIGH TEMPERATURE: 250°F


REPEATABILITY @ AMBIENT

STEP	NORMALIZED	STEP	NORMALIZED
0%	0.036	0%	0.063
100%	4.979	100%	4.992
FSO	4.943	FSO	4.929

STEP	OUTPUT 1	OUTPUT 2
0%	-0.010	-0.009
100%	4.974	4.975
FSO	4.984	4.984

### ERROR DISTRIBUTION



SUMMARY		CONNECTIONS		MISC
ZERO BALANCE	-0.008	PIN	DESCRIPTION	CONNECTOR
FULL SCALE OUTPUT	4.984	A	EXC+	202031
STATIC ACCURACY (%FSO)	0.040	D	EXC-	CAL REC. NO.
THERMAL ZERO SHIFT (%FSO / AMB TO HOT PER °F)	0.007	B	PSIG+	41912.56585
THERMAL ZERO SHIFT (%FSO / AMB TO COLD PER °F)	0.012	C	PSIG-	QA STAMP
THERMAL FSO SHIFT (%FSO / AMB TO HOT PER °F)	-0.006	E	TSIG+	
THERMAL FSO SHIFT (%FSO / AMB TO COLD PER °F)	-0.011	F	TSIG-	
				9/30/2014

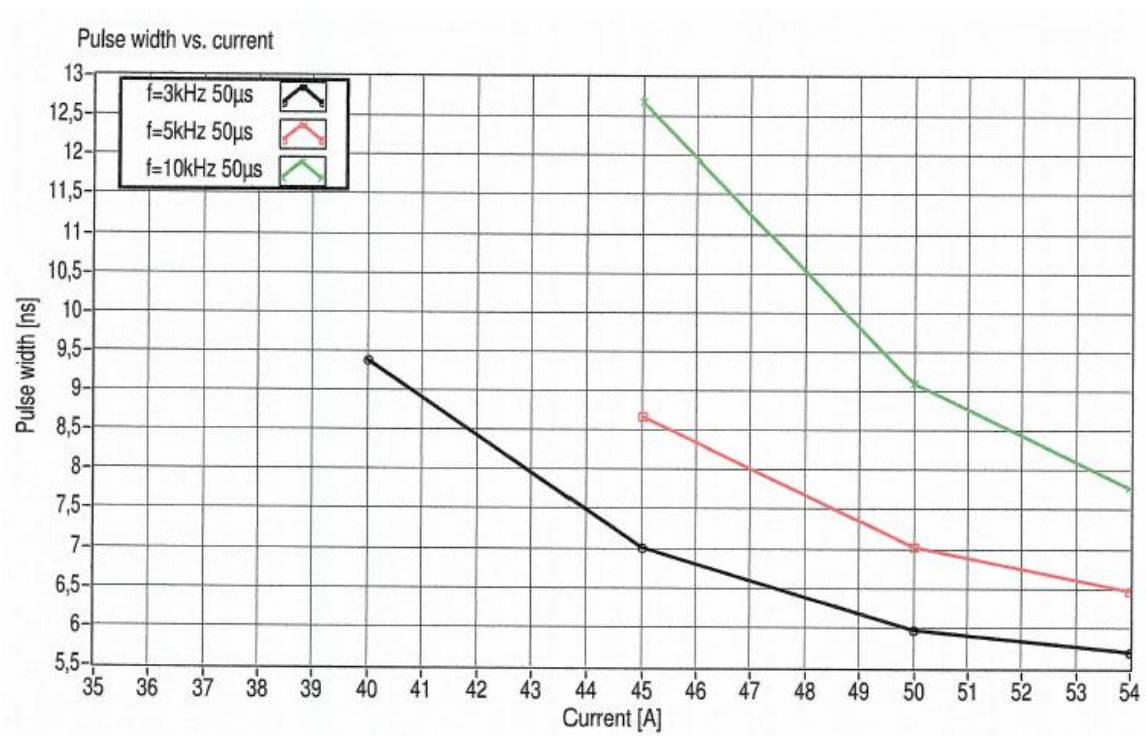
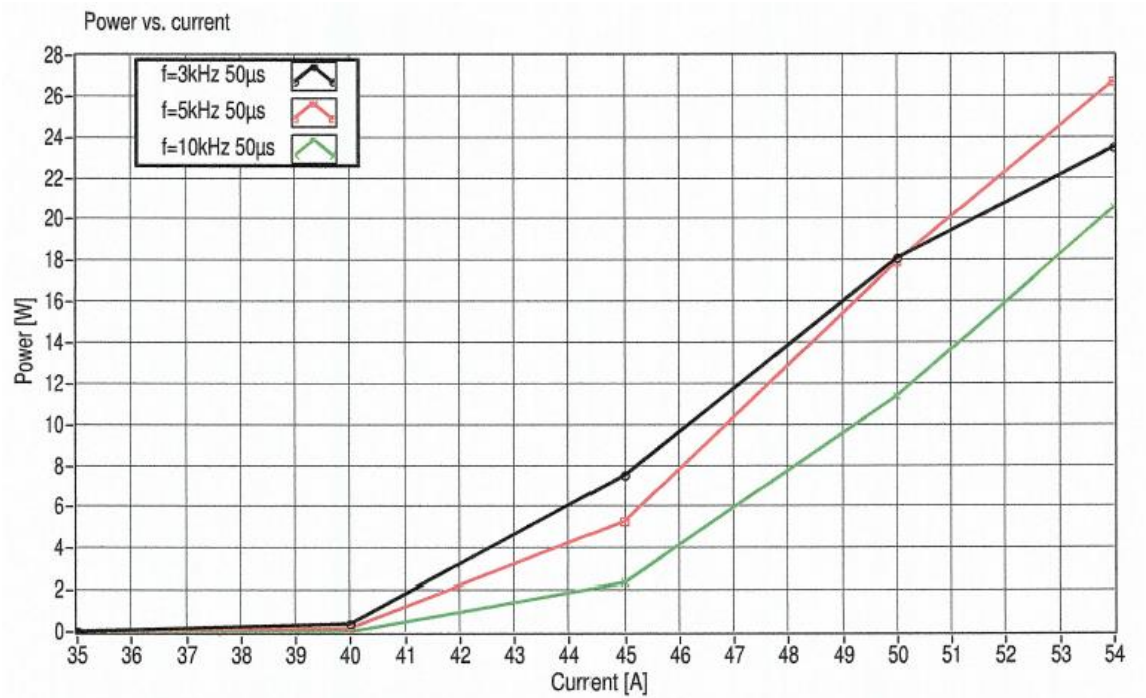
DCN 0628

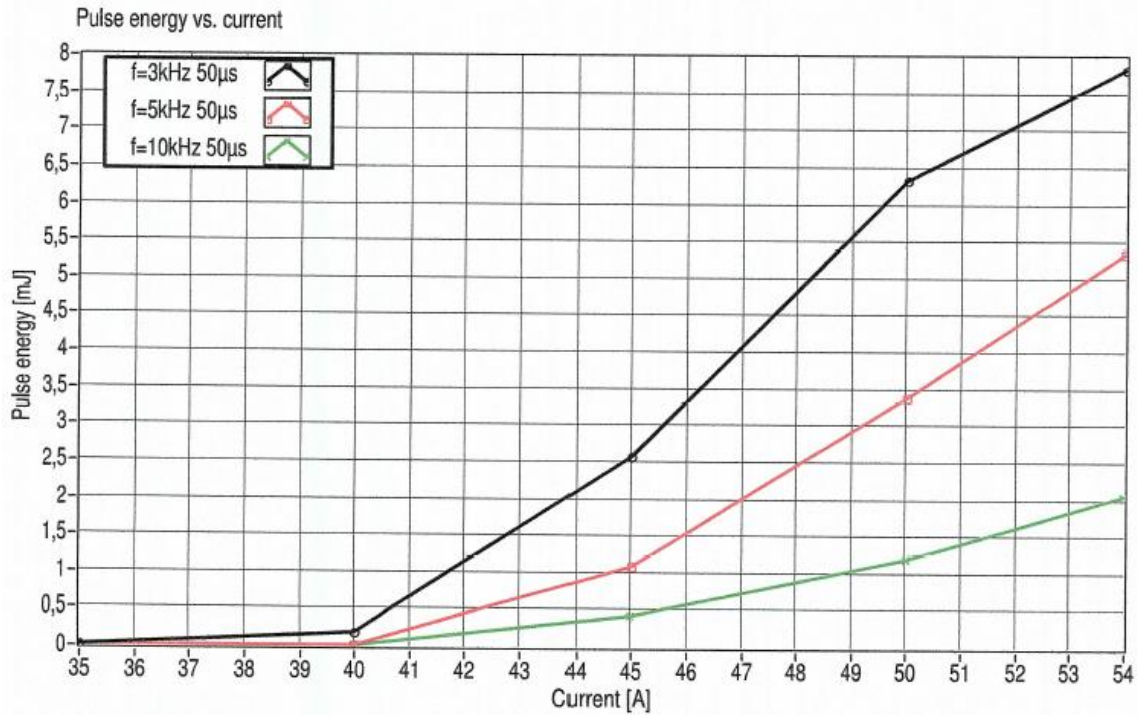
2112/001

## Appendix II

Specification of PLIF laser and Image Intensifier.

### Laser power sheet





Frequency	35 A	40 A	45 A	50 A	54 A
$f=3\text{kHz } 50\mu\text{s}$	0,00 W	0,37 W	7,53 W	18,10 W	23,47 W
$f=5\text{kHz } 50\mu\text{s}$	0,00 W	0,18 W	5,30 W	17,95 W	26,68 W
$f=10\text{kHz } 50\mu\text{s}$	0,00 W	0,00 W	2,35 W	11,38 W	20,52 W

Frequency	35 A	40 A	45 A	50 A	54 A
$f=3\text{kHz } 50\mu\text{s}$		9,4 ns	7,0 ns	6,0 ns	5,7 ns
$f=5\text{kHz } 50\mu\text{s}$			8,7 ns	7,0 ns	6,5 ns
$f=10\text{kHz } 50\mu\text{s}$			12,7 ns	9,1 ns	7,8 ns

Frequency	35 A	40 A	45 A	50 A	54 A
$f=3\text{kHz } 50\mu\text{s}$	0,01 mJ	0,18 mJ	2,56 mJ	6,32 mJ	7,82 mJ
$f=5\text{kHz } 50\mu\text{s}$	0,01 mJ	0,01 mJ	1,08 mJ	3,38 mJ	5,34 mJ
$f=10\text{kHz } 50\mu\text{s}$	0,01 mJ	0,01 mJ	0,42 mJ	1,19 mJ	2,05 mJ



●Image intensifier

Parameter		C10880-01C	C10880-03F	Unit
Luminous sensitivity (Typ.)		230		$\mu\text{A/lm}$
Radiant sensitivity (Typ.) <sup>1)</sup>		53		$\text{mA/W}$
Quantum efficiency (Typ.) <sup>1)</sup>		15		%
Photocathode window material		Synthetic quartz		-
Photocathode material		Multialkali		-
Spectral response range		185 to 900		nm
Wavelength of maximum response		430		nm
Photocathode diameter		25 <sup>4)</sup>		mm
Input lens mount		C-mount	F-mount	
Phosphor screen window material		Glass		-
Phosphor screen material		P-46		-
Luminous gain (Typ.)		$1 \times 10^5$		$(\text{lm/m}^2)/\text{lx}$
Radiant emittance gain (Typ.) <sup>1)</sup>		$4.2 \times 10^3$		$(\text{W/m}^2)/(\text{W/m}^2)$
EBI (lumen) (Typ.) <sup>2)</sup>		$2 \times 10^{-9}$		$\text{lm/cm}^2$
EBI (radiant) (Typ.) <sup>1) 2)</sup>		$2 \times 10^{-14}$		$\text{W/cm}^2$
Limiting resolution (Typ.)		38		Lp/mm
Image magnification		0.67		-
Maximum input light intensity (Typ.)	<sup>3)</sup>	$5.0 \times 10^{-3}$		lx
	<sup>1) 3)</sup>	$8.0 \times 10^{-10}$		$\text{W/cm}^2$

### Appendix III

#### Sample calculations

In order to prevent **choking**, we analyze the required cross sections needed for the piping section. Since the minimum operating pressure is 3 bar, then the upstream pressure must be calculated to find what the minimum value of pressure along with flow rate must be after the compressor. The pressure before the chamber can be found by treating it as an isentropic, compressible flow in a nozzle. From literature:

Air at  $M = .5$

$$\frac{P_t}{P_0} = .8483 \rightarrow P_0 = .8483/300000 = 353648Pa$$

This can be used as the final pressure after the heating section. Next we calculate the pressure drop after the heating section (assumed to be 3m max)

Initially at the compressor:

$$\dot{V}_{max} = 190 \text{ cfm} \left( .08976 \frac{m^3}{s} \right), P_{max} = 140 \text{ psig} (9.853 \text{ bar}),$$

$$T = 300K \text{ (slight heating)}, Ma < 1$$

$$v = \frac{\dot{V}_{max}}{A} = \frac{.08976}{.000196} = 457.873m/s$$

Since the velocity along the pipe is higher than  $Ma=1$ , then flow is choked.

To prevent this, then the flow after the heating section must be considered since it will have a higher velocity than that at the inlet.

After heating:

$$\rho = 3.925 \text{ kg/m}^3$$

$$Pr = .67$$

$$\mu = 2.707 \times 10^{-5} \text{ kg/m} \cdot \text{s}$$

$$g = 9.81m/s^2$$

$$c_p = 1032 \text{ J/kgK}$$

$$K = .0415w/mK$$

$$A = .000196m^2$$

$$\beta = 1/396.5$$

$$v = \frac{\dot{m}}{\rho A} = \frac{.344715}{3.925(.000196)} = 448.089m/s$$

$$Ma = \frac{v}{c} = \frac{448.089}{\sqrt{1.4(287)(500)}} = .99$$

We want  $Ma < 1$  (.8 max);

$$d = \sqrt{\frac{4\dot{m}}{\pi\rho Ma\sqrt{kRT}}} \approx .7''$$

A diameter of 0.7'' or greater will prevent choking.

Fanno line flow equations:

$$T_0 = T_0^*$$

$$\frac{P_0}{P_0^*} = \frac{\rho_0}{\rho_0^*} = \frac{1}{Ma} \left( \frac{2 + (k-1)Ma^2}{k+1} \right)^{(k+1)/2(k-1)}$$

$$\frac{P}{P^*} = \frac{\rho_0}{\rho_0^*} = \frac{1}{Ma} \left( \frac{k+1}{2 + (k-1)Ma^2} \right)^{1/2}$$

$$\frac{T}{T^*} = \frac{\rho_0}{\rho_0^*} = \left( \frac{k+1}{2 + (k-1)Ma^2} \right)$$

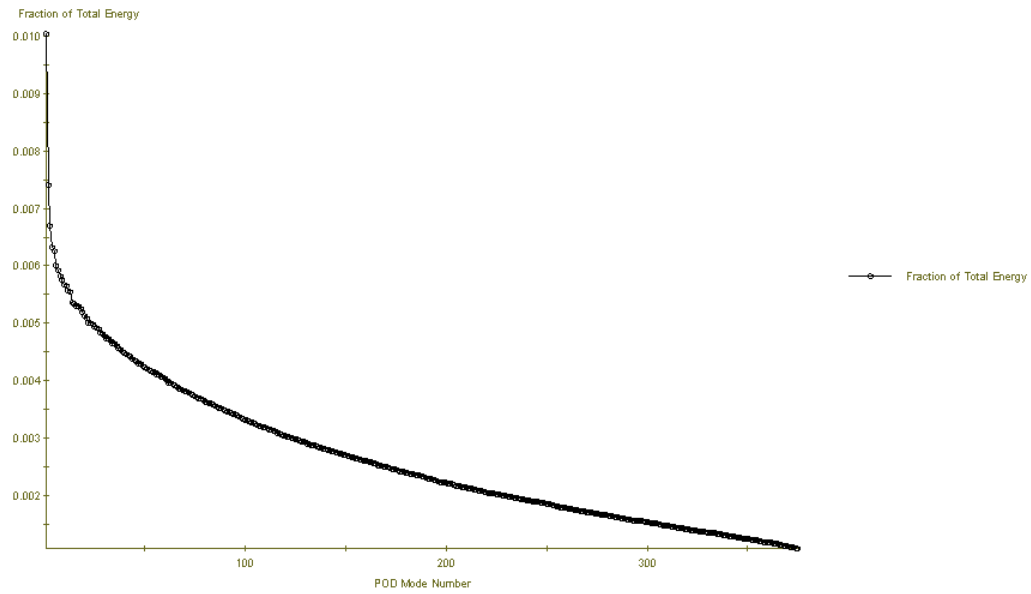
$$\frac{V}{V^*} = \frac{\rho^*}{\rho} = \frac{1}{Ma} \left( \frac{k+1}{2 + (k-1)Ma^2} \right)^{1/2}$$

$$\frac{fL^*}{D} = \frac{1 - Ma^2}{kMa^2} + \frac{k+1}{2k} \ln \left( \frac{(k+1)Ma^2}{2 + (k-1)Ma^2} \right)$$

## Appendix IV

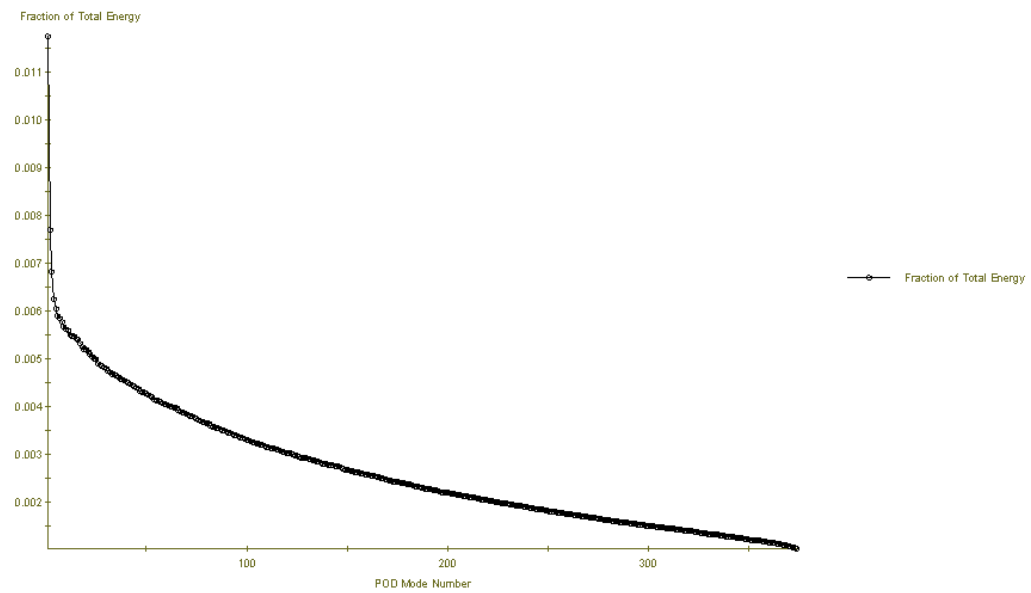
### POD snapshots

Modal Energy Distribution



POD snapshot for BR 67%  $Re = 22321$

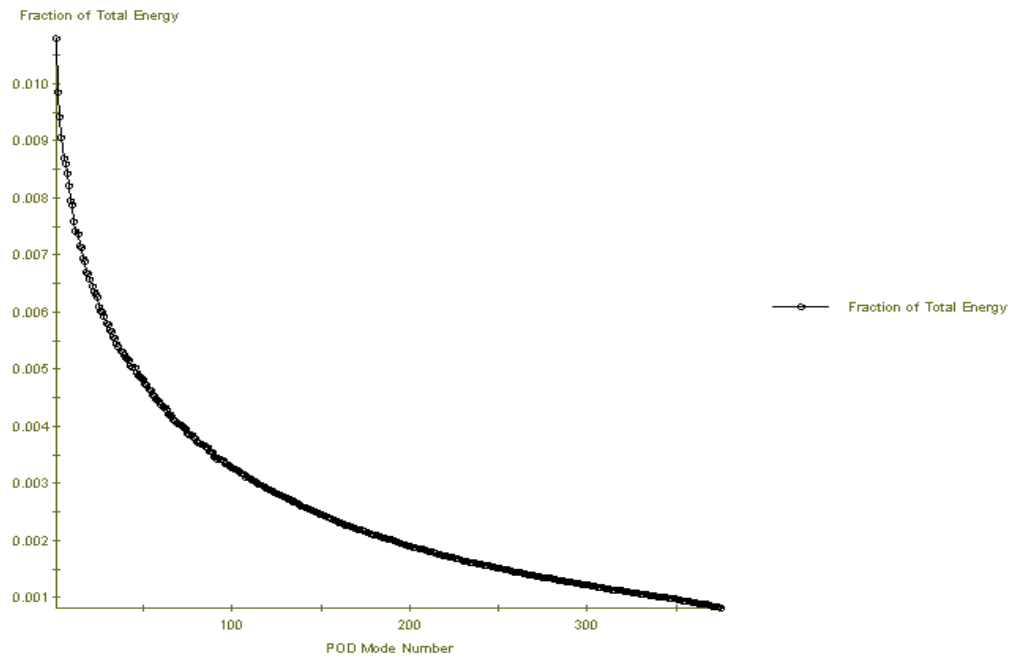
Modal Energy Distribution



POD snapshot for BR 67%  $Re = 10675$

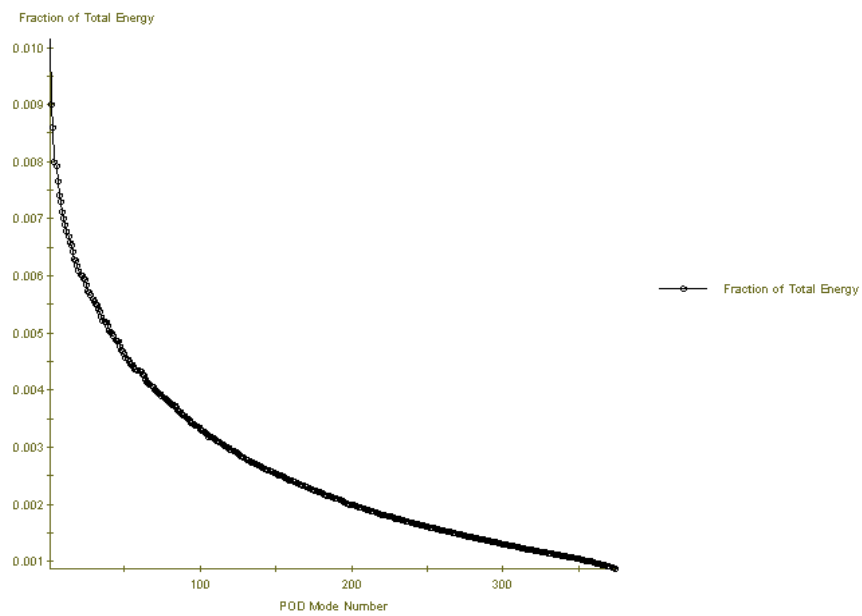


### Modal Energy Distribution



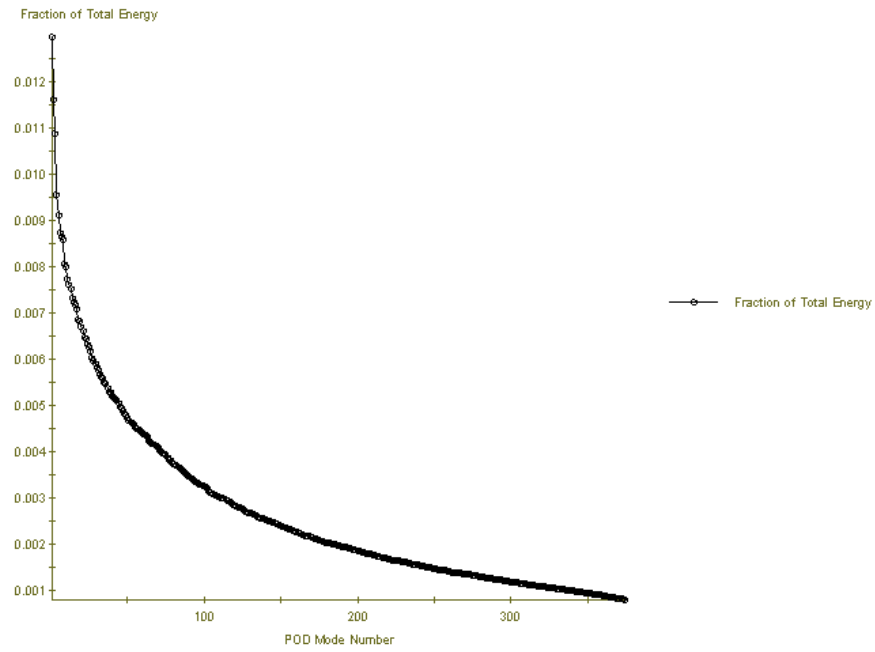
POD snapshot for BR 61%  $Re = 24413$

### Modal Energy Distribution



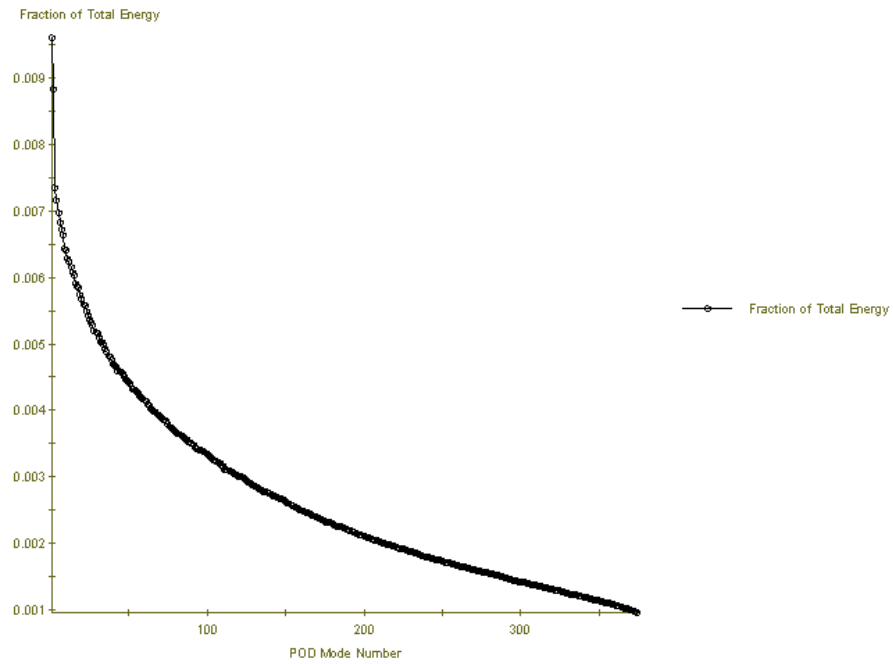
POD snapshot for BR 61%  $Re = 11676$

Modal Energy Distribution



POD snapshot for BR 54%  $Re = 26506$

Modal Energy Distribution



POD snapshot for BR 54%  $Re = 12676$

## Glossary

(In order of appearance)

Symbol	Description
$Re$	Reynolds number
$U$	Characterisrtic velocity
$L$	Characteristic length
$\nu$	Viscosity
$u$	Instantaneous velocity
$u'$	Fluctuation of velocity
$u_{rms}$	Root mean square value of velocity
$I$	Turbulent intensity
$TKE$	Turbulent kinetic energy
$\eta$	Kolmogorov length scale
$\varepsilon$	Energy dissipation
$t_\eta$	Kolmogorov time scale
$u_\eta$	Kolmogorov velocity
$\nu$	Fluid viscosity
$\eta$	Kolmogorove length scale
$t_\eta$	Kolmogorove time scale
$Re_T$	Turbulent Reynolds number
$Da$	Damkohler number
$Ka$	Karlovitz number
$L_T$	Integral length scale
$\delta_T$	Flame thickness
$S_L$	Laminar flame speed
$M$	Macn number
$\dot{Q}$	Heat flow per unit mass
$\dot{m}$	Mass flow rate
$c_p$	Specific heat
$A_s$	Surface area
$h$	Convection heat transfer coefficient
$T$	Temperature
$\alpha$	Thermal expansion coefficient
$k$	Thermal conductivity constant

## **Vita**

Marco Efrain Quiroz was born in El Paso, Texas on April 4<sup>th</sup>, 1991. He lived in Ciudad Juarez, Chihuahua until moving to El Paso in 1997. He completed his high school education at Montwood High School and began enrollment at The University of Texas at El Paso in the fall of 2009. He then completed his bachelor's in Mechanical Engineering in spring 2013 graduating in the top 10 of this class. He enrolled in the UTEP mechanical engineering graduate program and began doing research on turbulent flow and combustion at the cSETR the following summer, during which time he had two publications and presented these publications. He hopes to become a contributing member to not only the engineering community, but to society as well. His dream is to become involved in the next engineering breakthrough to supersede the internal combustion engine.

Permanent address: 3049 Oak Crest Cir.

El Paso, Texas, United States 79936

This thesis was typed by Marco Efrain Quiroz.